



# Two-phase flow, heat and mass transfer and tracer transport to the atmosphere from underground nuclear cavities through fractured porous media

Aliaksei Pazdniakou, Valeri Mourzenko, Jean-François Thovert, Pierre Adler, Eric Pili

## ► To cite this version:

Aliaksei Pazdniakou, Valeri Mourzenko, Jean-François Thovert, Pierre Adler, Eric Pili. Two-phase flow, heat and mass transfer and tracer transport to the atmosphere from underground nuclear cavities through fractured porous media. Pure and Applied Geophysics, 2022, 10.1007/s00024-022-03038-4 . hal-03828836

**HAL Id: hal-03828836**

**<https://hal.science/hal-03828836>**

Submitted on 24 Nov 2022

**HAL** is a multi-disciplinary open access archive for the deposit and dissemination of scientific research documents, whether they are published or not. The documents may come from teaching and research institutions in France or abroad, or from public or private research centers.

L'archive ouverte pluridisciplinaire **HAL**, est destinée au dépôt et à la diffusion de documents scientifiques de niveau recherche, publiés ou non, émanant des établissements d'enseignement et de recherche français ou étrangers, des laboratoires publics ou privés.

April 14, 2022

# **Two-phase flow, heat and mass transfer and tracer transport to the atmosphere from underground nuclear cavities through fractured porous media**

Aliaksei Pazdniakou<sup>1</sup>, Valeri Mourzenko<sup>2</sup>, Jean-François

Thovert<sup>2</sup>, Pierre M. Adler<sup>1</sup>, and Eric Pili<sup>3</sup>

<sup>1</sup>*Sorbonne Université, 4 place Jussieu, 75252 Paris Cedex 05*

<sup>2</sup>*Institut Pprime, CNRS, SP2MI, Futuroscope Chasseneuil and*

<sup>3</sup>*CEA, DAM, DIF, F-91297 Arpaçon, France*

## **Abstract**

Underground nuclear explosions generate non-isothermal two-phase flows, heat and mass transfer, and tracer transport through fractured porous media. The governing equations of these coupled phenomena on the Darcy scale are presented and the corresponding numerical code is briefly described. Two configurations are considered. In the first one, the damaged zone generated by the explosion is replaced by equivalent macroscopic boundary conditions at the bottom of the medium. Vapor condensation at distance from this zone plays a crucial role and slows down the tracer transport to the ground surface, while the presence of hot liquid water and of hot rubble particles in it accelerates it. In the second configuration, the damaged zone itself is treated as a porous medium with specific properties and is integrated in the simulation domain. Several regions can be distinguished with different properties, such as the chimney, the cavity, the solidified magma, the fractured porous medium, and the intact porous medium. Phase change, heat transfer and tracer transport can be detailed in these regions and at the boundaries between them. Among the most important conclusions, the role of phase change, of the thermal properties and therefore of the temperature, is pointed out.

## I. INTRODUCTION

An underground nuclear test generates extreme pressures and temperatures which induce dramatic mechanical damage to the host rock and strong flows of water, vapor and air together with production of various nuclides among which gaseous species such as radioxenon play a particular role for remote detection (Sun et al, 2015; Carrigan et al, 2016 and 2019). The objective of this work is to analyze the transport and transfer aspects of these complex phenomena when the host rock has reached a stable state.

The following ingredients are necessary in order to perform a realistic modeling. Three compressible fluids, namely air, water and its vapor, should be considered with heat and mass transfer. Therefore, the temperature field should be determined by solving an energy conservation equation. Moreover, the test generates radioactive elements which are carried by the fluids to the atmosphere. Finally, these transport and transfer occur through a medium with heterogeneous properties including a fractured porous matrix.

These are the general requirements. In addition, the numerical formulation should be sufficiently flexible to account for various boundary conditions and for variable distributions of the petrophysical characteristics of the medium, such as the porosity, the permeability, and the fracture density. For instance, the same code should be able to cope with the early-time conditions after rock stabilization when pressure and temperature are high and the long term behaviour when barometric pumping due to minute variations of the atmospheric pressure become predominant.

The following short literature review is devoted to transport of radionuclides from a nuclear cavity after an explosion from the point of view of its modeling. With a few exceptions such as Sun et al (2015) and Carrigan et al (2016, 2019), the thermal effects are neglected and only the long-term evolution is analyzed when barometric pumping is predominant.

A few papers use a simplified approach usually based on Nilson et al (1991) in order to easily obtain orders of magnitude. The configurations are composed of a single vertical fracture or of a series of such fractures periodically arranged. The transport equations are then solved in these configurations (Harp et al, 2019, 2020).

However, most papers use the dual permeability approach of Barenblatt et al (1960) with various degrees of sophistication and various softwares depending on their institutes. NUFT is used for single phase flows by Sun and Carrigan (2014) and for two-phase flows the thermal

effects are neglected and only long-term by Sun and Carrigan (2014, 2016), Sun et al (2015) and Guillon et al (2016). FEHM is used by Jordan et al (2014, 2015), Harp et al (2018), and Bourret et al (2020) for instance. Other codes are used by Lowrey et al (2013, 2015).

The methodology adopted here is very different since the exact geometry and properties of the fracture network are taken into account as was done by Mourzenko et al (2014) for barometric pumping. Of course, the computation cost is significantly increased, but a much more precise quantification of the phenomena is possible.

This paper which is a continuation of the companion paper (Pazdniakou et al, in preparation) is organized as follows. Section II provides the basic partial differential equations governing the phenomena on the Darcy scale, and the necessary constitutive equations. Theoretical details and the numerical methodology are exposed in the Appendices. The two studied configurations are detailed in Section III where the effect of an underground nuclear explosion on the host rock is first described. The applications to tracer transport from a damaged zone replaced by approximate boundary conditions at the bottom of the simulation domain are presented in Section IV. The difference between two-phase flow with and without phase change is analyzed, as well as the influence of liquid water and of an additional heat capacity in the damaged zone due to the presence of rubble particles. Results relative to a damaged zone which belongs to the simulation domain are presented in Section V. The damaged zone is first uniformly heated with uniform properties, and the influence of evaporation is outlined. Then, results relative to a damaged zone with heterogeneous properties and initial temperatures are summarized. Finally, some conclusions are given in Section VI.

## II. GENERAL

In this section, the basic equations governing the tracer transport by a fully compressible non-isothermal flow inside a fractured porous matrix are formulated. They are based on two major assumptions, namely the validity of the description on the Darcy scale, and local equilibrium.



## A. Two phase flow

In this model, a tracer is transported by the flow of two distinct phases. The liquid wetting phase denoted by the subscript  $w$  is naturally associated with liquid water which is generally present underground under normal conditions. The gaseous non-wetting phase denoted by the subscript  $n$  corresponds to air. While the air itself is a mixture of gases, for our model it is important to distinguish between dry air (subscript  $a$ ) and water vapor (subscript  $v$ ) due to water evaporation. Two phase flow takes place inside the porous matrix (subscript  $m$ ) as well as inside the fractures (subscript  $f$ ). The equations are very close to the ones used by Bogdanov et al (2003a).

Both, liquid and gaseous phases obey the mass conservation equations inside the porous matrix

$$\frac{\partial \varepsilon_m \rho_w (1 - S_n)}{\partial t} + \nabla \cdot \rho_w \bar{\mathbf{v}}_w = E_m \quad (1a)$$

$$\frac{\partial \varepsilon_m \rho_n S_n}{\partial t} + \nabla \cdot \rho_n \bar{\mathbf{v}}_n = -E_m \quad (1b)$$

where  $\varepsilon_m[-]$  is the matrix porosity,  $\rho_\alpha[\text{ML}^{-3}]$  the density of phase  $\alpha$ ,  $S_\alpha[-]$  the saturation,  $\bar{\mathbf{v}}_\alpha[\text{LT}^{-1}]$  the mean seepage velocity, and  $E_m[\text{ML}^{-3}\text{T}^{-1}]$  the phase transition source term associated with evaporation/condensation.

Inside the fractures, similar equations are written

$$\frac{\partial b \varepsilon_f \rho_w (1 - S_n)}{\partial t} + \nabla_S \cdot \rho_w \mathbf{q}_w + [\rho_w \bar{\mathbf{v}}_w] \cdot \mathbf{n} = E_f \quad (2a)$$

$$\frac{\partial b \varepsilon_f \rho_n S_n}{\partial t} + \nabla_S \cdot \rho_n \mathbf{q}_n + [\rho_n \bar{\mathbf{v}}_n] \cdot \mathbf{n} = -E_f \quad (2b)$$

where  $b$  [L] is the fracture aperture,  $\varepsilon_f[-]$  the fracture porosity (normally  $\varepsilon_f = 1$ ),  $\mathbf{q}_\alpha[\text{L}^2\text{T}^{-1}]$  the flow rate per unit width (integral of flow velocity over the fracture aperture), and  $E_f[\text{ML}^{-2}\text{T}^{-1}]$  the phase transition rate equivalent to a mass source or sink. Here,  $\nabla_S = (\mathbf{I} - \mathbf{nn}) \cdot \nabla$  denotes the two-dimensional gradient operator in the fracture plane, where  $\mathbf{n}$  the unit normal vector to the fracture, and  $\mathbf{I}[-]$  the unit tensor. The  $[\rho_\alpha \bar{\mathbf{v}}_\alpha] \cdot \mathbf{n}$  term describes the exchange between the fractures and the porous matrix, with  $[\zeta]$  denoting the difference between the values of an arbitrary quantity  $\zeta$  at the  $+\mathbf{n}$  and  $-\mathbf{n}$  sides of the fracture.

The mean seepage velocities  $\bar{\mathbf{v}}_\alpha$  are related to the flow driving forces (pressure gradient and gravity) by assuming the generalized Darcy laws

$$\bar{\mathbf{v}}_w = -\frac{K_{r,w}}{\mu_w} K_m (\nabla p_w - \rho_w \mathbf{g}) \quad (3a)$$

$$\bar{\mathbf{v}}_n = -\frac{K_{r,n}}{\mu_n} K_m (\nabla p_n - \rho_n \mathbf{g}) \quad (3b)$$

where  $K_{r,\alpha}[-]$  is the relative permeability,  $\mu_\alpha[\text{ML}^{-1}\text{T}^{-1}]$  the viscosity,  $K_m[\text{L}^2]$  the porous matrix permeability,  $p_\alpha[\text{ML}^{-1}\text{T}^{-2}]$  the pressure, and  $\mathbf{g}[\text{LT}^{-2}]$  the gravity acceleration.

The same considerations for the flow rates  $\mathbf{q}_\alpha$  for unit width of the fractures lead to similar Darcy's laws

$$\mathbf{q}_w = -\frac{\sigma_{r,w}}{\mu_w} \sigma_f (\nabla_S p_w - \rho_w \mathbf{g}_S) \quad (4a)$$

$$\mathbf{q}_n = -\frac{\sigma_{r,n}}{\mu_n} \sigma_f (\nabla_S p_n - \rho_n \mathbf{g}_S) \quad (4b)$$

where  $\sigma_f[\text{L}^3]$  is the fracture transmissivity,  $\sigma_{r,\alpha}[-]$  the relative fracture transmissivity;  $\mathbf{g}_S$  is given by  $\mathbf{g}_S = \mathbf{g} \cdot (\mathbf{I} - \mathbf{nn})$ . It is important to note that pressure is regarded as constant across the fracture aperture, and equal to the pressure in the matrix on either side (which implies  $[p] = 0$ ).

## B. Water vapor transport

In our model, the gaseous non-wetting phase  $n$  is a mixture of dry air  $a$  and water vapor  $v$ . For this binary mixture, the transport of the vapor component inside the porous matrix is described by the following convection-diffusion equation

$$\frac{\partial(\varepsilon_m S_n \rho_n C_v)}{\partial t} + \nabla \cdot (\bar{\mathbf{v}}_n \rho_n C_v) - \nabla \cdot (D_{mv} \bar{D}_n \rho_n \nabla C_v) = -E_m \quad (5)$$

where  $C_v[-]$  is the water vapor mass fraction,  $D_{mv}$  the molecular diffusion coefficient of the vapor, and  $\bar{D}_n$  is the effective diffusivity of the pore space occupied by the non-wetting phase. A similar convection-diffusion equation is formulated for the fractures and is given in Appendix A for the sake of brevity (A1).

The dry air mass fraction  $C_a$  can be simply derived from the additional relation

$$C_a + C_v = 1 \quad (6)$$

which holds everywhere.

This set of equations is well suited for  $C_v$  small or equal to 1. A more sophisticated approach for multi-component diffusion would require significant modifications of the model and is left outside the scope of the present study. Moreover, the vapor transport by diffusion is expected to be of little importance for the considered phenomena which are characterized

by steep spatial variations of temperature. High vapor concentrations ( $C_v \approx 1$ ) can only exist inside the limited overheated pressurized zone. Since it leaves this zone by convection and enters into the much cooler surrounding pore space, the vapor is very quickly condensed which decreases its concentration down to the ambient level ( $C_v \approx 0.012$ ).

### C. Energy transport

The energy transport influences all the phenomena included in the model. Heat transfer takes place by conduction and convection, while radiative transfer is ignored. The assumption of local thermal equilibrium implies the use of a single temperature  $T[\text{K}]$  for the solid  $T_s$ , gas  $T_n$ , and liquid  $T_w$  phase at a given point

$$T = T_s = T_n = T_w \quad (7)$$

Hence, the energy transport equations can be easily combined for all the phases present in the model. For the porous matrix, they yield

$$\begin{aligned} \frac{\partial}{\partial t} \{ \varepsilon_m [\rho_w(1 - S_n)h_w^* + \rho_n S_n h_n^*] + (1 - \varepsilon_m) \rho_s h_s^* \} + \nabla \cdot (\bar{\mathbf{v}}_w \rho_w h_w^* + \bar{\mathbf{v}}_n \rho_n h_n^*) \\ - \nabla \cdot (\lambda_m \nabla T) = R_m + \varepsilon_m \left[ (1 - S_n) \frac{\partial p_w}{\partial t} + S_n \frac{\partial p_n}{\partial t} \right] \end{aligned} \quad (8)$$

where  $h_\alpha^*[\text{L}^2\text{T}^{-2}]$  is the  $\alpha$  phase specific enthalpy,  $\lambda_m[\text{MLT}^{-3}\text{K}^{-1}]$  the effective conductivity of the porous matrix, and  $R_m[\text{ML}^{-1}\text{T}^{-3}]$  the energy source term corresponding to the phase change. The first term of the equation corresponds to the energy accumulation, the second to the energy transfer due to convection, and the third term to heat conduction. The last term of the equation on the right side corresponds to the combined contribution from the compression work and the viscous dissipation. Since constant specific heat capacities are assumed for all phases, the specific enthalpies are linear functions of temperature

$$h_s^* = c_s T \quad , \quad h_w^* = c_w T \quad , \quad h_n^* = (c_a C_a + c_v C_v) T \quad (9)$$

where  $c_\alpha[\text{L}^2\text{T}^{-2}\text{K}^{-1}]$  is the  $\alpha$  phase specific heat capacity at constant pressure.

For the fracture network, the temperature is considered constant across the fracture aperture and equal to the porous matrix temperature on either side. The resulting detailed equation is given by (A2).

## D. Tracer transport

The tracer is soluble in both the wetting and the non-wetting phases. In most cases, both phases are simultaneously present at a given location. Again an instantaneous local equilibrium between the tracer concentration inside the wetting phase  $\rho_w c_w^*$  and the non-wetting phase  $\rho_n c_n^*$  is supposed. Thus, the tracer concentrations are related through Henry's law

$$c_n^* \rho_n = K_D c_w^* \rho_w \quad (10)$$

where  $K_D$  is the gas-liquid distribution constant. With this relation, a new variable can be introduced

$$\tilde{C}^* = \frac{\rho_w(1 - S_n)c_w^* + \rho_n S_n c_n^*}{(1 - S_n)K_D^{-\frac{1}{2}} + S_n K_D^{\frac{1}{2}}} \quad (11)$$

which effectively characterizes tracer concentration whatever the number of phases present at a given location. The phase related concentrations can be easily recovered by using

$$c_w^* = \frac{\tilde{C}^*}{K_D^{\frac{1}{2}} \rho_w}, \quad c_n^* = \frac{K_D^{\frac{1}{2}} \tilde{C}^*}{\rho_n} \quad (12)$$

The denominator in (11) can be associated with the effective saturation

$$\tilde{S} = (1 - S_n)K_D^{-\frac{1}{2}} + S_n K_D^{\frac{1}{2}} \quad (13)$$

Also, an effective convective velocity inside the porous matrix and an effective convective flux inside the fractures can be defined as

$$\tilde{\mathbf{v}} = \bar{\mathbf{v}}_w K_D^{-\frac{1}{2}} + \bar{\mathbf{v}}_n K_D^{\frac{1}{2}} \quad (14a)$$

$$\tilde{\mathbf{q}} = \mathbf{q}_w K_D^{-\frac{1}{2}} + \mathbf{q}_n K_D^{\frac{1}{2}} \quad (14b)$$

Then, combining the individual tracer transport equations for wetting and non-wetting phases together and using the newly defined effective variables yields the single tracer transport equation for the porous matrix as

$$\frac{\partial \varepsilon_m \tilde{S} \tilde{C}^*}{\partial t} + \nabla \cdot \left[ \tilde{\mathbf{v}} \tilde{C}^* - \left( D_{mw} \bar{D}_w \rho_w \nabla \frac{\tilde{C}^*}{K_D^{\frac{1}{2}} \rho_w} + D_{mn} \bar{D}_n \rho_n \nabla \frac{K_D^{\frac{1}{2}} \tilde{C}^*}{\rho_n} \right) \right] = W_m \quad (15)$$

where  $\bar{D}_w$  is the effective diffusivity of the pore space occupied by the wetting phase,  $D_{mw}$  and  $D_{mn}$  are the tracer molecular diffusion coefficients for the wetting and the non-wetting

phase, respectively;  $W_m$  is the tracer source term. This equation can be solved for the effective concentration  $\tilde{C}^*$ , irrespectively of the phase distribution inside the simulation domain.

A similar equation holds inside the fractures (A3). The terms  $W_m$  and its counterpart in fractures  $W_f$  are included in the general code, but are taken equal to zero in this work; they could be used to take into account radon emanation for instance.

## E. Constitutive equations

Several constitutive equations must be supplied to complete the model.

### 1. State equations

The compressibility of the wetting phase is taken into account by a linear equation of state

$$\rho_w = \rho_{w,0} [1 + C_w (p_w - p_{w,0})] \quad (16)$$

where  $C_w$  [ $\text{Pa}^{-1}$ ] is the wetting fluid compressibility, and  $\rho_{w,0} = 1000 \text{ kg m}^{-3}$  is a reference density at a reference pressure  $p_{w,0} = 1 \text{ bar}$ . For water,  $C_w$  is very low and of the order of  $10^{-10} \text{ Pa}^{-1}$ . Unfortunately, the influence of temperature was not taken into account.

For the gaseous phase, the equation of state of ideal gases is adopted

$$\rho_n = \rho_a + \rho_v = \frac{p_n}{RT(C_a/M_a + C_v/M_v)} \quad (17)$$

where  $R_g = 8.3145 \text{ J K}^{-1} \text{ mol}^{-1}$  is the ideal gas constant,  $M_a = 0.02896 \text{ kg mol}^{-1}$  the dry air molar mass, and  $M_v = 0.01801528 \text{ kg mol}^{-1}$  the water vapor molar mass.

### 2. Capillary pressure and relative permeabilities

The pressures inside the wetting and the non-wetting phases are related one to another by the capillary pressure  $p_{ca}$  as

$$p_{ca} = p_n - p_w \quad (18)$$

The relation between the capillary pressure  $p_{ca}$  and the wetting fluid saturation  $S_w$  is described by van Genuchten (1980)

$$S_{w\beta} = \left[ 1 + \left( \frac{p_{ca}}{p_{0\beta}} \right)^{n_\beta} \right]^{\frac{1}{n_\beta} - 1}, \quad p_{ca} = p_{0\beta} \left[ S_{w\beta}^{\frac{n_\beta}{1-n_\beta}} - 1 \right]^{\frac{1}{n_\beta}}, \quad (\beta = m, f) \quad (19)$$

where  $p_{0\beta}$  and  $n_\beta$  are model parameters which define the shape of the capillary pressure curve. In addition, the relative permeabilities  $K_{r,i}$  and transmissivities  $\sigma_{r,i}$  are modeled as

$$K_{r,w} = S_{wm}^{\frac{1}{2}} \left[ 1 - \left( 1 - S_{wm}^{\frac{n_m}{n_m-1}} \right)^{1-\frac{1}{n_m}} \right]^2, \quad K_{r,n} = S_{nm}^{q_m} \quad (20)$$

$$\sigma_{r,w} = S_{wf}^{\frac{1}{2}} \left[ 1 - \left( 1 - S_{wf}^{\frac{n_f}{n_f-1}} \right)^{1-\frac{1}{n_f}} \right]^2, \quad \sigma_{r,n} = S_{nf}^{q_f} \quad (21)$$

Obviously, the model parameters  $p_{0\beta}, n_\beta$  and  $q_\beta$  are different in the porous matrix and the fractures. The very same equations were used by Bogdanov et al (2003b). The possible difficulties close to  $S_w = 0$  are discussed in Appendix B.

### 3. Effective diffusion coefficients

The effective diffusivities of the pore space occupied by the wetting  $\bar{D}_w$  and non-wetting  $\bar{D}_n$  phases can be expressed by

$$\bar{D}_w = \bar{D}_m S_w, \quad \bar{D}_n = \bar{D}_m S_n \text{ with } \bar{D}_m = \varepsilon_m^{1.4} \quad (22)$$

where  $\bar{D}_m$  is the effective diffusivity of the porous medium approximated by Archie's law (see Adler, 1992).

The effective diffusional conductivities of the fracture volume occupied by the wetting  $\bar{\Sigma}_w$  and non-wetting  $\bar{\Sigma}_n$  phase can be defined as (see Appendix A)

$$\bar{\Sigma}_w = \bar{\Sigma}_f S_w, \quad \bar{\Sigma}_n = \bar{\Sigma}_f S_n \text{ with } \bar{\Sigma}_f = b \quad (23)$$

where  $\bar{\Sigma}_f$  is the fracture diffusional conductivity for a plane channel of constant aperture  $b$  (Adler et al, 2012).

The effective conductivities of the porous matrix and of the fractures are approximated as

$$\lambda_m = \frac{\lambda_{U,m} + \lambda_{L,m}}{2}, \quad \Lambda_f = b \frac{\lambda_{U,f} + \lambda_{L,f}}{2} \quad (24)$$

where  $\lambda_{L,\eta}$  and  $\lambda_{U,\eta}$  ( $\eta=m,f$ ) are the lower and the upper Hashin-Shtrikman bounds calculated by taking into account the solid, the wetting and the non-wetting phases.

## F. Evaporation/condensation source term

The evaporation/condensation phenomenon can be naturally taken into account by using the source terms  $E_\alpha$  and  $R_\alpha$  which describe mass and energy effects, respectively.

For water, liquid and vapor phases are distinguished below the critical point at  $p_C=221.2$  bar and  $T_C=647.3$  K. The energy variation  $\Delta H_w$  due to evaporation/condensation can be expressed as a function of temperature (Reid et al, 1987)

$$\Delta H_w = [7.08\tau^{0.354} + 10.95\omega\tau^{0.456}] RT_C \quad [\text{J mol}]^{-1} \quad (25)$$

where  $\omega$  is the acentric factor ( $\omega=0.344$  for water), and  $\tau = 1 - T/T_C$ .

Evaporation/condensation takes place when there is a difference between the water vapor pressure

$$p_v = R \frac{\rho_v}{M_v} T \quad (26)$$

and the saturation vapor pressure at a given temperature (Reid et al, 1987)

$$p_{sv} = p_C e^{\frac{T_C}{T} (-7.76451\tau + 1.45838\tau^{1.5} - 2.7758\tau^3 - 1.23303\tau^6)} \quad (27)$$

The net mass flux due to phase change per unit area of liquid/vapor interface can be evaluated by the Hertz-Knudsen-Schrage equation. It is proportional to  $p_{sv} - p_v$  and sufficient to provide or extract enough vapor from the gas in the neighboring interstitial space to bring the partial pressure back to its equilibrium value in much less than 1 second, i.e. much less than the typical time step for the simulations. For this reason, the exchange terms  $E_m$  and  $E_f$  are modeled as

$$E_m = -\frac{1}{\delta t} \epsilon_m S_n \left( \frac{(p_{sv} - p_v) M_v}{RT} \right) \left[ 1 - 2^{-\frac{\delta t}{t_{0.5, \alpha}}} \right] \quad (28a)$$

$$E_f = -\frac{1}{\delta t} b \epsilon_f S_n \left( \frac{(p_{sv} - p_v) M_v}{RT} \right) \left[ 1 - 2^{-\frac{\delta t}{t_{0.5, \alpha}}} \right] \quad (28b)$$

Let us first ignore the factors within brackets.  $\delta t$  [s] is the time step. Obviously, these original source terms are devised to bring to zero the difference between the local water vapor and saturation vapor densities during one time step. The energy source terms corresponding to the phase change for the porous medium  $R_m$  and for the fractures  $R_f$  can be easily defined as

$$R_m = \frac{E_m \Delta H_w}{M_v} \quad ; \quad R_f = \frac{E_f \Delta H_w}{M_v} \quad (29)$$

In order to improve the numerical stability of the code, the factors within brackets were added where  $t_{0.5,\alpha}$  [s] is a time scale parameter which can be set separately for evaporation  $t_{0.5,e}$  and condensation  $t_{0.5,c}$ . Further details are given in Appendix B.

### III. THE STUDIED CONFIGURATIONS

First, this section provides the main characteristics of the underground medium after the explosion. Then, this medium is schematized by two configurations. The more complete one is called configuration with an internal damaged zone (CIDZ). The nuclear cavity and the chimney, previously called the damaged zone, that developed after the nuclear explosion are viewed as a porous medium with specific properties, surrounded by the host rock and prolonged up to the surface by a fractured porous medium; the evolution of this zone which may include solidified magma is computed with the rest of the domain; the subscript c will denote the quantities relative to this zone. A simplification of the previous one is called configuration with boundary conditions (CBC) since the damaged zone generated by the explosion is now included in the computations by some overall conservation relations and by the boundary conditions imposed at the bottom of the fractured porous medium.

The physical properties and parameters for both configurations are summarized in Table I. For the calculations, the same initial tracer mass fraction inside the damaged zone  $c_n^* = 0.1$  is imposed and the concentration fields and curves which are represented correspond to this condition. However, it must be noted that due to the different initial conditions inside the damaged zone (gas pressure and temperature), the initial total mass of tracer varies from case to case. For the analysis, it is important to note that all the obtained tracer fluxes are rescaled to the same initial tracer mass  $M_c = 15$  g which can be safely done due to the linearity of the tracer transport equation; for  $^{133}\text{Xe}$ , this mass corresponds to ca. 0.1 mol or  $10^{17}$  Bq.

#### A. General

As the phenomenology of underground nuclear explosions is beyond the scope of this work, we will here only refer to a given finite geometry with given properties. Johnson (1959), Boardman (1964), Derlich (1970) and Carothers (1995) provide more details on phenomenol-



ogy. As an example, the list of the United States nuclear tests (DOE/NV-209, 2015) shows the diversity of the underground nuclear test configurations. For demonstration purposes, an energy of 150 kt is considered, which corresponds to the upper boundary of the energy range assigned to nuclear tests conducted after 1973, following the Treaty on the Limitation of Underground Nuclear Weapon Tests (DOE/NV-209, 2015). As presented by Boardman (1964), a 150 kt-explosion at a depth of 630 meters in a granitic rock would produce a cavity with a radius of ca. 50 meters (hence a volume of ca.  $5 \times 10^5 \text{ m}^3$ ) and develop a chimney with an height of ca. 230 m filled with rubbles. The chosen characteristics (energy, depth of burial, rock type) and assumed geometrical and thermodynamic consequences (volume of cavity, height of chimney, initial pressure and temperature) do not represent any particular existing nuclear test. They rather represent a paradigm with realistic features including high gradients and long distances to demonstrate the robustness of the code as well as to provide relevant lessons regarding what controls tracer gas emission to the atmosphere. At the final stage schematized in Fig. 1, we assume that a fracture network reach the ground surface, thus creating a percolating fractured porous medium located over the chimney, which provides a path for the hot pressurized gas potentially emitted to the atmosphere before any detection. This network is not included in what is called the damaged zone.

The main purpose of this study is to apply the developed code to the tracer transport simulation from the damaged zone through a fractured porous medium aiming at a close replication of the conditions corresponding to the final stage of an underground nuclear test. The influence of various factors, such as the conditions inside the damaged zone (gas pressure and temperature), and some others will be considered and discussed.

It should be stressed that the permeabilities chosen here are much smaller than the ones of Carrigan et al (2016, 2019, 2020), simply because the fields of applications are different. The same is true for the other parameters such as the chimney permeability, the domain dimensions and some of the physical conditions. Indeed, most studies addressed the peculiarly high permeability and high porosity volcanic rocks from the Nevada National Security Site (NNSS, USA) with their nonetheless peculiar joints and fracture systems due to the formation mode of these rocks (e.g. Carrigan et al., 1996, 2016, 2019; Bourret et al., 2020). Only few studies addressed low permeability volcanic rocks at the NNSS (Carrigan et al, 2020). We therefore focused our efforts on low permeability and low porosity crystalline rocks, taking benefit from a long record of studies of the rock properties conducted at the

Roselend Natural Laboratory (Richon et al., 2005; Patriarche et al., 2007; Pili et al., 2008; Guillon et al., 2013). This remains relevant to the field of nuclear testing considering that crystalline rocks (gneiss, granite, diorite) compose the basement of the Democratic People's Republic of Korea nuclear test site in Pungye-ri (Coblentz and Pabian, 2015).

## B. Configuration with an internal chimney (CIDZ)

This configuration displayed in Fig. 1 contains the cavity, the chimney, possibly a solidified magma, the fractured porous medium located above the chimney, and the assumed intact porous medium enveloping them. The geometry of these elements can be varied at will. Here, the full simulation domain is a parallelepipedon of size  $200 \times 200 \times 650 \text{ m}^3$  with properties depending on position. The permeability of the porous matrix is  $K_m = 10^{-16} \text{ m}^2$ , and its porosity is  $\varepsilon = 0.01$  which are close to the properties of a granite rock. The damaged zone located inside the porous medium is also a parallelepiped of size  $100 \times 100 \times 200 \text{ m}^3$ . It is often modeled as a uniform porous medium (in which case it is a chimney) with a much higher permeability  $K_c = 8.33 \times 10^{-8} \text{ m}^2$  and a porosity  $\varepsilon = 0.29$ . The fracture network (see Fig. 1b) consists of 192 regular hexagonal fractures of radius 20 m. On the four vertical sides and on the bottom one, the damaged zone is surrounded by an intact porous medium which is 50 m thick (see Fig. 1a). The centers of the fractures are randomly generated inside the  $100 \times 100 \times 400 \text{ m}^3$  domain located over the chimney. The fracture network percolates along the  $z$ -axis, i.e., it continuously connects the chimney and the ground surface. The fracture aperture  $b = 10^{-3} \text{ m}$  is constant with a transmissivity  $\sigma_f = 8.33 \times 10^{-11} \text{ m}^3$ .

All the computations are initiated assuming normal physical conditions inside the domain around the damaged zone. The normal physical conditions correspond to the temperature  $T_0 = 288.15 \text{ K}$ , the gas pressure  $p_0 = 101330 \text{ Pa}$ , and the gas density  $\rho_0 = 1.2172 \text{ kg} \cdot \text{m}^{-3}$  ( $C_v = 0.0104$ ). The initial water saturation inside the domain is  $S_w = 0.242$ .

Dirichlet boundary conditions corresponding to the normal state are applied at all the sides of the simulation domain. The ground surface corresponds to the upper side of the simulation domain  $z = 650 \text{ m}$  where Dirichlet boundary conditions for the temperature  $T(z = 650) = 288.15 \text{ K}$ , the tracer mass fraction  $c_n^*(z = 650) = 0$ , and the atmospheric pressure are imposed. The atmospheric pressure at the soil surface undergoes periodic

variations

$$p(z = 650) = p_n(z = 650) = p_0 + A_p \sin(\omega_p t) \quad (30)$$

with an amplitude  $A_p = 10^3$  Pa, and a frequency  $\omega_p = 10^{-5}$  Rad·s<sup>-1</sup> which corresponds to a period of 7.27 days. This model pressure, although very simplified, captures most of the characteristics of a natural signal (amplitude and frequency).

Various initial conditions inside the damaged zone are studied with the gas pressure ranging between 1.21 and 27.48 bar, and the temperature between 378.15 and 1000 K. Water saturations inside the chimney vary between 0 and 0.0672. Initially, the gas inside the chimney is almost exclusively composed of water vapor ( $C_v = 0.99$ ).

### C. Configuration with boundary conditions (CBC)

In order to accelerate the computational speed, the simulation domain of Fig. 1 can be simplified as displayed in Fig. 2a where it contains the fractured porous medium located over a surface where approximately equivalent boundary conditions corresponding to the damaged zone, i.e. the chimney and the cavity, are imposed. For the sake of simplicity, the ensemble cavity plus chimney is designated by the term chimney in this configuration.

The simulation domain is reduced to a parallelepipedon of size  $100 \times 100 \times 400$  m<sup>3</sup>. The permeability of the porous matrix is  $K_m = 8 \times 10^{-14}$  m<sup>2</sup>, and its porosity is  $\varepsilon_m = 0.05$ . The fracture network inside the domain (see Fig. 2b) consists of 147 regular hexagonal fractures of radius 20 m. This fracture network which is at the percolation threshold percolates along the three directions of space. The same equivalent aperture  $b = 10^{-3}$  m is assigned to all the individual fractures, which implies a fracture transmissivity  $\sigma_f$  equal to  $8.33 \times 10^{-11}$  m<sup>3</sup>. As a result (cf [28]), the effective permeability of this fractured porous medium is  $K_{eff} = 3.78 \times 10^{-13}$  m<sup>2</sup> when calculated with spatially periodic boundary conditions.

The initial conditions inside the simulation domain are assumed to be normal. The temperature is  $T_0 = 288.15$  K and the air pressure  $p_0 = 101330$  Pa. The gas density is  $\rho_0 = 1.2172$  kg m<sup>-3</sup> since it includes some vapor ( $C_v = 0.0104$ ). The initial water saturation throughout the domain is  $S_w = 0.27$ , except for  $100 < z < 200$  m, where it is slightly increased to  $S_w = 0.30$ .

The chimney is replaced by boundary conditions applied at  $z = 0$  m. It is characterized by a volume  $V_c = 100 \times 100 \times H_c$  m<sup>3</sup> filled with a heated pressurized gas containing a tracer

and optionally some amount of liquid water.  $V_c$  corresponds to the volume of the pore space between the rubble particles after the collapse of the initial spherical cavity. Here,  $H_c = 50$  m resulting in  $V_c = 5 \times 10^5 \text{ m}^3$ . The chimney is also characterized by the heat capacity coefficient  $C_c$  which is associated with the total heat capacity of the rubble particles inside it, but it is possible to set  $C_c = 0$  for a cavity without rubble particles. The exchanges between the chimney and the fractured porous matrix take place through all the bottom surface of area  $S_b = 10000 \text{ m}^2$ .

For simplicity, a no flow boundary condition for the liquid phase is applied at  $z=0$ ; this is likely to be true due to the high pressure inside the chimney for all the simulations. However, the water and vapor contained inside the chimney can evaporate or condense according to the prevailing physical conditions. Thus, the evolution of the water density inside the chimney can be expressed by

$$\frac{d\rho'_{w,c}}{dt} = \frac{E_c}{V_c} \quad (31)$$

where  $E_c$  is the phase change source term for the chimney given in  $\text{kg s}^{-1}$ , and  $\rho'_{w,c} = M_{water}/V_c$  the density relative to the chimney volume  $V_c$ . The water saturation inside the chimney is obtained as

$$S_{w,c} = \frac{\rho'_{w,c}}{\rho_{w,0} [1 + C_w (p_{w,c} - p_{w,0})]} \quad (32)$$

where  $p_{w,c}$  is the pressure inside the water phase. The capillary pressure inside the chimney is supposed to be zero, hence  $p_{w,c} = p_{n,c}$ . The pressure inside the gas phase  $p_{n,c}$  follows from the equation of state for perfect gases. Evolution of the gas density  $\rho_{n,c}$  inside the chimney is calculated from

$$\frac{d[\rho_{n,c}(1 - S_{w,c})]}{dt} = \frac{Q_{n,b} - E_c}{V_c} \quad (33)$$

where  $Q_{n,b} \text{ kg s}^{-1}$  is the total gas flux from the porous medium to the chimney at the bottom side of the simulation domain (i.e., the gas flux integrated over the bottom surface). Similarly, the mass fraction of the vapor  $C_{v,c}$  in the gas inside the chimney is computed from

$$\frac{d[C_{v,c}\rho_{n,c}(1 - S_{w,c})]}{dt} = \frac{Q_{v,b} - E_c}{V_c} \quad (34)$$

where  $Q_{v,b} \text{ kg s}^{-1}$  is the total vapor flux at the bottom side of the simulation domain. The evolution of the effective tracer concentration  $\tilde{C}_c^*$  inside the chimney is given by

$$\frac{d[\tilde{C}_c^*(S_{w,c}K_D^{-\frac{1}{2}} + (1 - S_{w,c})K_D^{\frac{1}{2}})]}{dt} = \frac{Q_{c,b} + W_c}{V_c} \quad (35)$$

where  $Q_{c,b}$   $\text{kg s}^{-1}$  is the total tracer flux at the bottom side of the simulation domain, and  $W_c$   $\text{kg s}^{-1}$  is the tracer source term for the chimney, which is usually zero.

Finally, the evolution of the temperature  $T_c$  inside the chimney should take into account the heat stored in the solid rubble particles. Therefore,

$$\frac{d[C_c + \rho'_{w,c}c_w V_c + \rho_{n,c}(1 - S_{w,c})c_n V_c]T_c}{dt} = V_c \frac{dp_{n,c}}{dt} + Q_{T,b} + E_c \Delta H_w \quad (36)$$

where  $Q_{T,b}$  [W] is the total heat flux at the bottom side of the simulation domain, and  $C_c$  the heat capacity of the rubble particles.  $T_c$  should not be confused with the critical temperature  $T_C$  in (25).  $Q_{T,b}$  and  $Q_{v,b}$  are oriented as  $Q_{n,b}$  from the porous medium to the chimney.

The oscillating atmospheric pressure (30) is imposed at the ground surface.

Spatially periodic boundary conditions are applied at the lateral sides of the simulation domain.

Various initial ( $t = 0$  s) conditions inside the chimney were considered. In most simulations, the desired conditions inside the chimney ( $p_c = 2 \times 10^7$  Pa,  $T_c = 1000$  K) are characterized by very high pressures and temperatures which induce numerical difficulties alleviated by a gradual initial increase of the gas pressure inside the chimney instead of using an instantaneous peak value. The variations of  $p_c$  are of the form

$$p_c = 10^5 + na\delta t \text{ with } a \approx 2.5 \times 10^8 \quad \delta t = 8 \times 10^{-4} \quad (37)$$

Thus, the chimney pressure  $p_c = 2 \times 10^7$  Pa can be reached after  $n = 100$  time steps  $\delta t$  at  $t = 8 \times 10^{-2}$  s. Since this initial stage of the simulation associated with the pressure increase inside the chimney constitutes only a tiny time fraction of the total simulated time period, the pressure increase can be considered as almost instantaneous.

After the desirable pressure level is obtained, the pressure growth is stopped, and the time step is gradually increased to the desirable value ( $\delta t = 800$  s) or to the maximal value which can be supported by the code without divergence. Then, the simulation proceeds as usually with gas, heat, and tracer leaving the chimney and propagating through the fractured porous medium.

## IV. APPLICATIONS TO CONFIGURATIONS WITH BOUNDARY CONDITIONS (CBC)

This section summarizes the simulations performed for the configurations with boundary conditions (CBC) by using the two-phase flow model.

### A. Two phase flow without phase change

Of course, it is unrealistic to neglect phase change for such high initial pressures, but this artificial situation roughly corresponds to a single phase compressible gas flow from a heated pressurized chimney. In addition, it sets an upper limit for the expected tracer flux at the ground surface for given pressure and temperature inside the chimney and illustrates the necessity to consider the vapor condensation effects.

The initial chimney temperature is  $T_c = 1000$  K and the initial gas pressure  $p_c = 2 \times 10^7$  Pa. The chimney volume is  $V_c = 5 \times 10^5$  m<sup>3</sup>;  $C_c$  is set to 0 J K<sup>-1</sup>. Without any loss of generality, the initial tracer mass fraction inside the chimney is set to  $c_n^* = 0.1$ . The simulation is performed with  $g = 0$ . The gas inside the chimney is mainly the water vapor  $C_{v,c} = 0.98$ . The air is initially dry inside the domain  $C_v = 0$ . The initial saturation is  $S_w = 0.025$ , except for  $100 < z < 200$  m where it is set to  $S_w = 0.2425$ .

The spatial variations of  $p_n$ ,  $\rho_n$ ,  $S_w$ ,  $T$ ,  $C_v$  and  $c_n^*$  at  $t = 2.68$  days are displayed in Fig. 3. Generally, these profiles resemble those obtained for single phase flow [30].  $S_w(z)$  is almost unchanged by the gas flow. The water vapor and the tracer easily penetrate into the porous matrix, which generates an almost uniform profile considering their respective mass fractions. The layer of higher water saturation for  $100 < z < 200$  m only slightly delays the tracer transport to the ground surface.

The evolution of the gas pressure, the temperature, the water saturation, the vapor and the tracer mass fractions as well as the total tracer mass inside the chimney are presented in Fig. 4. Again,  $p_{n,c}$  and  $T_c$  inside the chimney are rapidly decreasing in the same manner as for the single phase simulations [30]. The vapor and tracer mass fractions inside the chimney can be considered as constant during the simulation. Fig. 4f shows that the tracer initially present only inside the chimney rapidly leaves it with the gas.

The tracer flux evolution at the ground surface as well as the fraction of tracer mass

released to the atmosphere are displayed in Fig. 5. The tracer flux evolution at the ground surface is very similar to the one for single phase with similar initial conditions inside the chimney [30]. The tracer arrives very quickly at the ground surface. Its flux reaches a maximum around  $t = 0.267$  day and then rapidly decreases. More than 50 % of the tracer are released to the atmosphere during the first two days.

For the sake of completeness, radionuclide activities (Bq) have been added to Fig. 5. However, converting radionuclide activities (Bq) released to the atmosphere into volume activity ( $\text{Bq m}^{-3}$ ) measured at a given monitoring station depends on the situations, notably the distance of the emission from the stations, the wind direction and speed as well as the dispersive properties of the atmosphere at the time, in addition to the minimum detectable concentration of the station (e.g., Achim et al., 2020; Topin et al., 2020). This is thus beyond the scope of the present study.

## B. Two phase flow with phase change

In order to demonstrate the effects of the phase change, calculations were performed with the same initial conditions as in the previous case, but taking into account the phase change. The time scale parameters are set to  $t_{0.5,e} = t_{0.5,c} = 80$  s.

The distributions of  $p_n$ ,  $\rho_n$ ,  $S_w$ ,  $T$ ,  $C_v$  and  $c_n^*$  at  $t = 0.2$  days are displayed in Fig. 6. When compared to the case without phase change, a very different picture is observed. Now, the gas, which is initially mainly composed of the water vapor, travels a relatively short distance before being condensed since the surrounding porous matrix is cold. Hence, the pressure and the density profiles quickly decrease for  $z$  small. This sharp decrease designates the areas where condensation takes place. Due to condensation,  $S_w$  grows inside the fractures and inside the porous matrix as well. This process effectively decreases the permeability of the fractured porous medium; this effect coupled with the pressure losses slows down the tracer transport toward the ground surface. Moreover, because of the massive vapor condensation,  $T$  increases further away from the chimney with variations up to several tens of degrees in the fractures and in the surrounding porous matrix. The limits of the condensation zone are provided by the distribution of  $C_v$  in Fig. 6e. This zone is limited to  $z < 100$  m. Since the tracer stays mostly inside the gaseous phase, the vapor condensation locally increases the tracer mass fraction inside the gaseous phase (see Fig. 6f) to a great extent. The tracer

propagates inside the fractures and penetrates into the porous matrix as well.

The evolution of the main variables inside the chimney denoted by the subscript  $c$  is displayed in Fig. 4. Now,  $p_{n,c}$  decreases significantly faster, since the vapor is condensed in the vicinity of the chimney leading to a fast pressure drop. Hence, the gas is evacuated from the chimney significantly faster, thus increasing the transport rate of the tracer from the chimney. However, because of the low pressure outside the chimney, the tracer does not travel fast to the ground surface.  $T_c$  and  $\rho_c$  also decrease faster for the same reasons.  $C_{v,c}$  is almost constant with a slight trend to decrease, since the vapor continues condensing close to the chimney. For the same reasons,  $c_{n,c}^*$  only experiences a very slight increase.

At the present state of the simulation ( $t = 17950$  s), the tracer has not reached the ground surface, while in the absence of condensation (see Fig. 5a), the tracer flux has already reached its maximum and is decreasing.

### C. Influence of liquid water inside the chimney

If the initial conditions inside the chimney are less extreme, liquid water can be present. For this purpose, the initial chimney temperature is decreased to  $T_c = 502.15$  K, and the initial gas pressure is set to  $p_{n,c} = 27.48 \times 10^5$  Pa. The vapor mass fraction inside the chimney is  $C_{v,c} = 0.99$ , and the initial water saturation is  $S_w = 0.03828$ . The initial saturation is increased to  $S_w = 0.27$  everywhere inside the simulation domain, and to  $S_w = 0.3$  for  $200 < z < 100$  m. All the other parameters are the same.

The distributions of the main variables inside the simulation domain at  $t = 13.56$  days are displayed in Fig. 7. The profiles of  $p_n$  and  $\rho_n$  are quite similar to those of the previous section. Near the chimney,  $p_n$  experiences a large steep drop which is associated with vapor condensation, a phenomenon visible in the profile of  $C_v$  in Fig. 7e. The rest of the domain is filled with dry air mixed with a small amount of vapor. From the temperature profile, it follows that the heat is absorbed near the chimney, increasing the temperature not only inside the fractures, but also inside the porous matrix. This temperature increase causes water evaporation close to the chimney (see Fig. 7c). This evaporation also locally decreases  $c_n^*$ . In the rest of the porous matrix,  $c_n^*$  is significantly higher than inside the chimney due to vapor condensation. Thus, inside the fractures near the ground surface, it is up to 120 times higher than inside the chimney.



These effects are more visible in Fig. 8 where the variables inside the simulation domain are displayed in 3D. Thus, it is clear that water is evaporated from a relatively thin (about 5 m thick) layer next to the chimney. Right over this area, there is a thin highly water saturated layer.  $S_w$  is also significantly increased inside the fractures and inside the contiguous porous matrix. Moreover, high  $C_v$  can be found only near the chimney, and  $T$  increases where vapor is condensed and where  $c_n^*$  is the highest (see Fig. 8d).

The evolution of the main variables inside the chimney is presented in Fig. 4.  $p_c$  and  $T_c$  gradually decrease at a smaller rate due to the presence of water. The water present inside the chimney slowly evaporates, as can be observed in Fig. 4c. This process increases  $C_{v,n}$  (see Fig. 4d) and decreases  $c_n^*$  (see Fig. 4e). Fig. 4f shows that the tracer is rapidly transported from the chimney into the surrounding fractured porous medium.

The evolution of the tracer flux at the ground surface as well as the fraction of tracer mass released to the atmosphere are presented in Fig. 5. The total tracer flux (for the total initial tracer mass  $M_c=15$  g) at the ground surface exceeds the level of  $10^{-14}$  g s $^{-1}$  after  $t=5$  days.

In contrast with the case without vapor condensation (black solid line), the tracer flux is much smaller and steadily grows for several days. Due to the low gas pressure inside the fractured porous matrix, the tracer flows out to the atmosphere slowly, with less than 1% of the total tracer mass being released to the atmosphere after 13 days as demonstrated in Fig. 5b.

#### D. Influence of an additional heat capacity inside the chimney

In order to simulate the influence of rubble particles inside the chimney, an additional heat capacity  $C_c = 1.55 \times 10^{18}$  J K $^{-1}$  is introduced into the heat balance equation (36). All the other simulation conditions are the same as in the previous section.

Comparing the distributions of the variables inside the simulation domain at  $t = 8.6$  days (see Fig. 9) with the previous case at 13.2 days (see Fig. 8) where  $C_c = 0$ , it is clear that transports from the chimney are intensified by the additional heat capacity. Thus, there is much more condensed water inside the fractured porous matrix (see Fig. 9a), and the water was condensed further from the chimney. Moreover, the region next to the chimney, where water is vaporized, is approximately twice thicker than when  $C_c = 0$ . The temperature inside

the fractured porous matrix has risen more and further from the chimney (see Fig. 9b). The vapor condensation zone is also larger (see Fig. 9c). Finally, the tracer is more dispersed inside the fractured porous matrix (see Fig. 9d).

The variations of the main variables inside the chimney are shown in Fig. 4. Thanks to the very large additional heat capacity which stores a lot of heat, water is rapidly vaporized almost at a constant rate, and there is no more water inside the chimney after 3 days (see Fig. 4c). The evaporation rate is high enough to maintain an almost constant gas pressure inside the chimney when water still remains (see Fig. 4a); when evaporation is over, the pressure rapidly decreases. The absolute variations of  $T_c$  are very tiny due to the huge value of the additional heat capacity used in the simulation; therefore,  $T_c$  can be effectively considered as constant (see Fig. 4b).  $C_{v,c}$  increases during the water evaporation stage, then it decreases due to the air next to the chimney which goes back into the chimney (see Fig. 4d).  $c_{n,c}^*$  decreases when there is still water inside the chimney; then, it slightly increases due to the tracer next to the chimney which goes back into the chimney because of the air motion (see Fig. 4e).

Hence, there is almost no tracer left inside the chimney after 10 days (see Fig. 4f). This figure also shows that in presence of an additional heat capacity, which maximizes evaporation inside the chimney, the tracer transport out of the chimney is intensified compared to the previous case where only liquid water is present inside the chimney. This allows to conclude that the presence of the vapor source inside the chimney intensifies tracer transport from the chimney; this effect is positively correlated with the strength of this source.

The variations of the tracer flux at the ground surface and the fraction of tracer mass released to the atmosphere are given in Fig. 5. These plots are similar to those with  $C_c = 0$  (compare to the green dotted lines). However, the intensity of the tracer transport towards the ground surface is increased when  $C_c$  is not zero. Thus, the tracer flux reaches the level of  $10^{-14} \text{ gs}^{-1}$  roughly one day earlier, and it is 3.7 times higher at  $t = 9.82$  days. However, the tracer is transported to the atmosphere slowly, with less than 1.4% released after 10 days due to the low pressure inside the fractured porous medium, since all the vapor is condensed near the chimney.

## V. APPLICATIONS TO CONFIGURATIONS WITH AN INTERNAL DAMAGED ZONE (CIDZ)

Several simulations were performed in the second configuration described in section III B and displayed in Fig. 1; most simulations are for damaged zones restricted to a chimney, hence the notations;  $S_c$  and  $V_c$  are the chimney surface and volume for the CIDZ configuration, respectively. Only the initial conditions inside the chimney are different for the following CIDZ simulations, while the other parameters are the same as in Section IV.

### A. Uniformly heated chimney. Simulation without evaporation inside the chimney

First, consider an uniformly heated chimney with the following initial conditions identical to the ones for the CBC-simulations:  $T_c = 502.15$  K,  $p_{n,c} = 27.48 \times 10^5$  Pa,  $C_{v,c} = 0.99$ ,  $S_{w,c} = 0.03828$ , and  $c_{n,c}^* = 0.1$ . For this particular simulation, water evaporation is restricted inside the chimney by setting the corresponding source term to 0 if the local water saturation satisfies  $S_w \leq 0.05$ . However, water condensation is allowed inside the chimney.

The presence of the chimney inside the simulation domain allows to take into account physical phenomena inside it and at its border with the porous matrix which may influence the tracer outflow, but were not accounted for in the CBC-simulations. The distributions of  $S_w$ ,  $T$ ,  $C_v$  and  $c_n^*$  at  $t = 9.96$  hours are given in Fig. 10. The distribution of  $S_w$  in Fig. 10a shows that the vapor leaving the chimney is mainly condensed inside the fractured porous medium located over the chimney. Moreover, much less condensation is observed inside the intact porous matrix near the bottom and the lateral sides of  $S_c$ . Again, the vapor does not travel far from the chimney before being condensed as seen in Fig. 10c. Vapor condensation causes small temperature rises in the fractures. Heat is also transferred to the intact porous matrix at the bottom and the lateral sides of  $S_c$  (see Fig. 10b). Due to the vapor condensation, the tracer mass fraction  $c_n^*$  is increased inside the fractures and the contiguous porous matrix. It is also increased inside the intact porous matrix forming a quite thick layer surrounding  $S_c$ . It is interesting to note that  $c_n^*$  in  $V_c$  close to this layer is decreased. This can be explained by the evaporation of the water at  $S_c$ .

Various border effects can be better observed in the fields at  $t = 9.96$  hours in the vertical cross section  $y = 100$  as shown in Fig. 11. The distribution of  $S_w$  implies that water evap-

oration and condensation happen near  $S_c$  indicated by the white rectangle simultaneously inside and outside the chimney.  $C_v$  is also changed in that region while  $c_n^*$  is significantly increased inside the porous medium close to the fractures; it is also increased inside the layer of the intact porous medium surrounding  $V_c$  while inside it, it is decreased close to  $S_c$  due to evaporation. In the central part of the chimney, the tracer mass fraction is unaffected and is the same as at the beginning of the simulation. The gas pressure which is uniform in  $V_c$  drops abruptly outside the chimney due to the vapor condensation and to the low permeability of the intact porous matrix. Outside the condensation area,  $p_n$  is slightly increased in the fractures and the contiguous porous matrix. Temperature varies only near  $S_c$ .

The evolution of the mean values of the main variables inside the chimney is displayed in Fig. 17. Since there is no water evaporation inside  $V_c$ , the mean gas pressure decreases quite rapidly by leaving the chimney through the fracture network and through  $S_c$ . The mean temperature decreases slowly due to the high value of  $C_c$ . At this stage, temperature variations are caused by the cooling at  $S_c$ . In  $V_c$ ,  $S_w$  increases since some water can be condensed next to  $S_c$  as shown in Fig. 11. Water evaporation/condensation at  $S_c$  induces variations of  $C_v$  inside  $V_c$ . Due to the decrease of  $c_n^*$  near  $S_c$  (see Fig. 11), the mean tracer mass fraction in  $V_c$  also decreases. Fig. 17f implies that the tracer initially present only in  $V_c$  is being transported into the fractured porous medium, and that a significantly larger part of the tracer goes into the intact porous medium. This can be related to the high ratio between the areas of the chimney in contact with the intact porous matrix  $S = 9 \times 10^4 \text{ m}^2$  and the fractured porous medium  $S = 10^4 \text{ m}^2$ .

The tracer reaches the ground surface at  $t = 9.05$  hours. The variations of the tracer flux at the ground surface and the tracer mass released to the atmosphere are given in Fig. 12. The tracer flux grows steadily, however, it is still very limited, and the amount of the tracer transported to the atmosphere is very small at the current stage. Despite the small pressure gradient between  $V_c$  and the ground surface due to the vapor condensation, the tracer arrives to the ground surface significantly faster than in the similar CBC simulations. This can be explained by the better connectivity of the fracture network due to the increased number of fractures. Moreover, the decreased permeability of the porous matrix channels the flow inside the fractures which accelerates transport to the ground surface. Again, radionuclide activities have been added and the same comments as for Fig. 5 apply.

## B. Uniformly heated chimney. Simulation with evaporation inside the chimney

The simulation conditions are kept the same as in the previous section without the limitations on the evaporation inside  $V_c$ .

The distributions of the main variables at  $t = 1.71$  hours are presented in Fig. 13. Even after a shorter simulation time than in the previous case,  $S_w$  is increased to a higher extent around the chimney and inside the fractured porous matrix. These effects are certainly due to the water evaporation inside  $V_c$  which intensifies the gas outflow from the chimney. Heat transport was also intensified, though the observable effects are small. Despite a higher amount, the vapor is still quickly condensed near the chimney.  $c_n^*$  is quite different with almost no tracer in  $V_c$  since it is transported to the surrounding medium thanks to the water evaporation in  $V_c$ .

The distributions of the variables at  $t = 3.51$  hours in the cross section  $y = 100$  are displayed in Fig. 14. Again, considering the distribution of  $S_w$ , the effects of the evaporation and condensation near  $S_c$  are more intense.  $C_v$  is almost uniform except near  $S_c$ . Unlike the previous simulation,  $c_n^*$  is close to zero inside  $V_c$  at  $t = 3.51$  hours, and the tracer is mostly around  $V_c$  and in the fractures close to it. Thanks to water evaporation, the gas pressure is still 21.9 bar inside  $V_c$  after  $t = 3.51$  hours. As usually, the pressure drops very quickly outside the chimney. Temperature variations are still limited to  $S_c$ .

The evolution of the main average values inside  $V_c$  is presented in Fig. 17. After the simulation start,  $p_n$  inside  $V_c$  drops, but it is quickly restored by water evaporation inside  $V_c$ . Then,  $p_n$  slowly decreases due to the progressive cooling of the chimney observed in Fig. 17b which is faster than in the previous case. The mean water saturation in  $V_c$  first drops due to local water evaporation, but after some time it starts growing because of the water evaporation inside the neighbouring intact zone and the consequent vapor condensation at  $S_c$ .  $C_v$  inside  $V_c$  is now steadily increasing, while  $c_n^*$  rapidly decreases. From the last plot (see Fig. 17f), it is clear that the tracer quickly leaves the chimney, and most of it is trapped inside the intact porous medium, while a small fraction escapes through the fractured porous medium. When compared to the previous case without evaporation inside  $V_c$  (see the same Fig. 17f), it is clear that the tracer leaves the chimney much faster in presence of an evaporation source inside  $V_c$ . Thus, 87.09% and 11.8% of the initial tracer amount are transferred to the intact porous medium and the fractured porous medium,

respectively, for the case with evaporation inside the chimney after  $t = 0.113$  days, compared to the 61.91% and 6.92% for the case without evaporation after the same time.

At the current stage, the tracer is still inside the fractured porous matrix, i.e., there is no tracer flux at the ground surface.

### C. Chimney and magma

Actually, it is unlikely that the chimney is uniformly heated. Most of the heat released during the test is retained by the solidified magma in the lower part of the chimney, while its upper part filled with rock fragments is significantly cooler. The whole damaged zone is called again chimney.

Therefore, the initial temperature field inside the chimney is not uniform. The upper part (190 meters) is at  $T_c = 378.15$  K, while the magma (assumed 10 meters thick with a porosity  $\varepsilon = 0.01$ ) is at  $T_c = 1000$  K.  $S_w$  is  $S_w = 0.0672$  in the upper part and  $S_w = 0.025$  in the magma. The initial gas pressure  $p_{n,c} = 1.2086 \times 10^5$  Pa, the vapor mass fraction  $C_v = 0.99$ , and the tracer mass fraction  $c_n^* = 0.1$  are the same in both parts.

The distributions of the main variables inside the simulation domain are shown in Fig. 15. Since the gas outflow from the chimney is very weak due to the low pressure inside it, the vapor condensation is very limited outside  $V_c$  during the initial stage (see Fig. 15a). There is slightly more condensed water near the hot magma at  $t = 0.54$  days. However, when enough of the heat is transferred through  $S_c$ , the water inside the porous matrix near  $S_c$  starts evaporating. Then, the vapor can enter the chimney due to the much higher permeability of the latter, and it is condensed near  $S_c$ . There can be also some water flow effects caused by the significant difference in the capillary pressures inside  $V_c$  and inside the intact porous matrix. For these reasons, water saturation does not increase outside the chimney at  $t = 2.17$  days. At this stage, the vapor leaving the chimney is very quickly condensed in  $V_c$  near  $S_c$ , and only the air and the tracer leave the chimney. Moreover, there is slightly more air in the upper half of the chimney because of the initial intensive water evaporation in the magma. The temperature contrast inside the chimney is clearly seen in Fig. 15b. The magma remains very hot for a long time due to its high heat capacity and its low thermal conductivity. Temperature variations outside the chimney are negligible. Fig. 15d shows that the tracer is first pushed from the lower half of the domain into the upper half by the

massive water evaporation inside the overheated part of the chimney. Later, when the excess of the vapor is getting recondensed inside the cooler upper part of the chimney, the tracer slowly goes down through the chimney. Moreover, the tracer slowly leaves the chimney through the fracture network to be accumulated inside the intact porous medium near  $S_c$ .

The main distributions at  $t = 2.17$  days in the cross section  $y = 100$  are shown in Fig. 16.  $S_w$  is seen to decrease inside the porous medium around the chimney, and to increase inside  $V_c$  near  $S_c$ .  $S_w$  is zero in the hot magma where all the water is rapidly evaporated, and the water inside  $S_c$  near this zone is also being gradually evaporated. The vapor mass fraction is almost uniform, but slightly higher in the lower half of  $V_c$ . There is more air near  $S_c$ . It is clear that the tracer was pushed by the vapor to the upper part of  $V_c$ , and consequently to the fracture network and the intact porous medium. The tracer mass fraction is also higher in the regions where vapor condenses. At this stage, the gas pressure is almost uniform inside  $V_c$ , and it is slightly lower than its initial value due to the cooling of this zone. Outside  $V_c$ , the pressure is higher inside the fracture network, but the tracer transport is slow due to the low pressure difference. Again, temperature variations are very limited due to the high heat capacity and low heat conductivity of the solid phase.

The variations of the mean values of the main variables inside  $V_c$  are displayed in Fig. 17. At the beginning, the mean gas pressure inside  $V_c$  rapidly rises because of the evaporation inside the magma. Then, it slowly decreases due to the gas outflow from the chimney and because of the condensation of the excess vapor in the cooler part of the chimney. At the end, it is slightly lower than the initial value and it continues decreasing because of the chimney cooling. The mean temperature in  $V_c$  slowly decreases as observed in Fig. 17b. The mean saturation in  $V_c$  slowly increases due to the border effects, i.e., the water evaporated at the chimney border inside the intact porous medium is recondensed inside  $V_c$  near  $S_c$ . The mean vapor mass fraction inside  $V_c$  first drops since some air from the lateral sides of the chimney enters into the chimney during the initial stage. Then, mean vapor mass fraction constantly increases since the air leaves the chimney through the fracture network and is constantly replaced by vapor eventually reaching a maximum and beginning to decrease slightly.

The mean tracer mass fraction for the gas phase inside  $V_c$  decreases with time. First, it decreases rapidly due to the fast evaporation inside the hot magma. After that, it slowly decreases for the same reasons as for the dry air. The tracer distribution among the different

parts of the simulation domain shows that the tracer leaves the chimney and goes to the fractured porous medium and the intact porous medium. This time, the ratio between these quantities is smaller than in the previous simulation cases.

At this stage, there is no tracer flow at the ground surface.

## VI. CONCLUDING REMARKS

A number of simulations were started with various conditions in two different configurations. A simplified configuration (CBC) consists of a fractured porous matrix with boundary conditions at its bottom which take into account the influence of the chimney. In the second configuration (CIDZ), the simulation domain contains the chimney, the fractured porous medium over it, and the intact porous matrix surrounding them.

For the CBC configuration, the influence of evaporation/condensation is clearly demonstrated; it significantly slows down the tracer transport to the ground surface. Reversely, the presence of liquid water and rubble particles inside the chimney induces an additional heat capacity and intensifies the tracer transport out of the chimney, since water evaporation tends to increase pressure for a longer time.

Similar effects are observed for the CIDZ configuration with much more detail in the three regions, namely the chimney and the cavity, the fractured porous medium, and the intact porous medium, and at the boundaries between these regions. Moreover, a zone of hot solidified magma is added to the chimney and the cavity.

A few conclusions can be drawn from this preliminary work. First, all other things being equal, temperature controls the surface release of radioxenon for the range of parameters considered; for the same cavity volume and the same total mass of radioxenon inside the cavity, the total mass fraction released at the surface is larger for a larger heat capacity (presence of hot magma). Second, flow and transport inside the chimney may lead to redistribution of radioxenon inside the surrounding (fractured) porous medium, with consequences on the quantities of radioxenon and isotope inventory possibly released at the surface.

However, much work remains to be done. Together with the systematic study of the petrophysical parameters such as the fracture aperture, their density and diameter, a comparison should be made in the same conditions with the existing dual porosity models used by Carrigan et al (2016,2019,2020) for instance. This should result in a precise assessment of



the possibilities of these models which demand a much smaller computational effort. Finally, different configurations could be analyzed where for instance fractures could be present at the level of the chimney and generate complex two-phase behaviours.

**Acknowledgments:** This work was done in the framework of the CEA-Sorbonne Université collaboration CAJ.19-84. The authors thank Charles Carrigan and an anonymous referee for reviewing the manuscript, as well as Martin Kalinowski for editorial handling.

**Declaration:** No specific declaration

- 
- [1] Achim, P., Generoso, S., Topin, S., Gross, P., Monfort, M., Moulin, C., Le Petit, G., Douysset, G. & Morin, M. (2021). 6 months of radioxenon detection in western Europe with the SPALAX-New generation system – Part 2: Atmospheric transport modelling. *Journal of Environmental Radioactivity* 226, 106455.
  - [2] Adler, P.M. (1992). *Porous media: geometry and transports*. Butterworth/Heinemann.
  - [3] Adler, P.M., Thovert, J.-F., & Mourzenko V.V. (2012). *Fractured porous media*. Oxford University Press.
  - [4] Barenblatt, G.I., Zheltov, Iu.P., & Kochina, I.N. (1960). Basic concepts in the theory of seepage of homogeneous liquids in fissured rocks, *Soviet Appl. Math. Mech. (P.M.M.)*, 24, 852–864.
  - [5] Boardman, C.C., Rabb, D.D., & McArthur, R.D. (1964). Responses of Four Rock Mediums to Contained Nuclear Explosions. *Journal of Geophysical Research*, 69 3457–3469.
  - [6] Bogdanov, I., Mourzenko, V.V., Thovert, J.F., & Adler, P.M. (2003a). Two-phase flow through fractured porous media. *Phys. Rev. E* 68, 026703.
  - [7] Bogdanov, I., Mourzenko, V.V., Thovert, J.F., & Adler, P.M. (2003b). Effective permeability of fractured porous media in steady-state flow, *Water Resources Research*, 39, 10.1029/2001WR000756.
  - [8] Bourret, S.M., Kwicklis, E.M., Harp, D.R., Ortiz, J.P., & Stauffer, P.H. (2020). Beyond Barnwell: Applying lessons learned from the Barnwell site to other historic underground

- nuclear tests at Pahute Mesa to understand radioactive gas-seepage observations. *Journal of Environmental Radioactivity* 222, 106297.
- [9] Carrigan, C.R., Heinle R.A., Hudson G.B., Nitao J.J., & Zucca J.J. (1996). Trace gas emissions on geological faults as indicators of underground nuclear testing. *Nature* 382, 528–531.
  - [10] Carrigan, C.R., Sun, Y., Hunter, S.L., Ruddle, D.G., Wagoner, J.L., Myers, K.B.L., Emer, D.F., Drellack, S.L., & Chipman V.D. (2016). Delayed signatures of underground nuclear explosions. *Sci. Rep.* 6, 23032; doi: 10.1038/srep23032.
  - [11] Carrigan C.R., Sun, Y., & Simpson M.D. (2019). The Characteristic release of noble gases from an underground nuclear explosion. *J. Environ.Radioact.* 196, 91-97.
  - [12] Carrigan, C.R., Sun, Y., Hunter, S.L., Ruddle, D.G., Simpson, M.D., Obi, C.M., Huckins-Gang, H.E., Prothro, L.B., & Townsend, M.J. (2020). Gas transport across the low-permeability containment zone of an underground nuclear explosion. *Sci. Rep.* 10, 1437. <https://doi.org/10.1038/s41598-020-58445-1>.
  - [13] Carothers, J.E. (1995). Caging the dragon-The containment of underground nuclear explosions. U.S. Department of Energy, 726 p.
  - [14] Coblenz, D. and Pabian, F. (2015). Revised Geologic Site Characterization of the North Korean Test Site at Punggye-ri. *Science & Global Security* 23. 101–120.
  - [15] Derlich, S. (1970). Underground nuclear explosion effects in granite rock fracturing, Symposium on Engineering with Nuclear Explosive, Las Vegas, Nevada, pp. 505–518.
  - [16] Guillon, S., Vu, M.-T., Pili, E. and Adler, P.M. (2013). Field and numerical determinations of air permeability of unsaturated fractured porous rocks on various scales. *Water Resources Research* 49, 2801-2811.
  - [17] Guillon, S., Sun, Y., Purtschert, R., Raghoo, L., Pili, E., & Carrigan, C.R. (2016). Alteration of natural  $^{37}\text{Ar}$  activity concentration in the subsurface by gas transport and water infiltration. *Journal of Environmental Radioactivity* 155-156, 89–96.
  - [18] Harp, D.R., Ortiz, J.P., Pandey, S., Karra, S., Anderson, D., Bradley, C., Viswanathan, H., & Stauffer, P.H. (2018). Immobile Pore-Water Storage Enhancement and Retardation of Gas Transport in Fractured Rock, *Transp Porous Med* 124, 369–394, /doi.org/10.1007/s11242-018-1072-8.
  - [19] Harp, D.R., Ortiz, J.P., & Stauffer, P.H. (2019). Identification of dominant gas transport frequencies during barometric pumping of fractured rock. *Scientific Reports* 9, 9537.

- [20] Harp, D.R., Bourret, S.M., Stauffer, P.H., & Kwicklis, E.M. (2020). Discriminating Underground Nuclear Explosions Leading To Late-Time Radionuclide Gas Seeps. *Geophysical Research Letters* 47, e2019GL086654.
- [21] Harten, A (1993). High Resolution Schemes for Hyperbolic Conservation Laws. *Journal of Computational Physics*, 49, 357.
- [22] Huseby, O., Thovert, J.-F., & Adler, P.M. (1997). Geometry and topology of fracture systems, *Journal of Physics A: Mathematical and Theoretical*, 30, 1415–1444.
- [23] Johnson, G.W., Higgins, G.H., & Violet, C.E. (1959). Underground nuclear detonations. *Journal of Geophysical Research* 64, 1457–1470.
- [24] Jordan, A.B., Stauffer, P.H., Zyvoloski, G.A., Person, M.A., MacCarthy, J.K. and Anderson, D.N. (2014). Uncertainty in Prediction of Radionuclide Gas Migration from Underground nuclear Explosions. *Vadose Zone Journal* 13, 1–13.
- [25] Jordan, A.B., Stauffer, P.H., Knight, E.E., Rougier, E., & Anderson, D.N. (2015). Radionuclide Gas Transport through nuclear Explosion-Generated Fracture Networks. *Scientific Reports* 5, 18383.
- [26] Lowrey, J.D., Biegalski, S.R., Osborne, A.G., & Deinert, M.R. (2013). Subsurface mass transport affects the radionuclide signatures that are used to identify clandestine nuclear tests. *Geophysical Research Letters* 40, 111–115.
- [27] Lowrey, J.D., Osborne, A.G., Biegalski, S.R., & Deinert, M.R. (2015). Comparison of Numerically Stable Methods for Implementation of a Double Porosity Model with First-Order Reaction Terms. *Transport in Porous Media* 106, 33–45.
- [28] Mourzenko, V.V., Varloteaux, C., Guillon, S., Thovert, J.-F., Pili, E., & Adler, P.M. (2014). *Barometric pumping of a fractured porous medium*, *Geophys. Res. Lett.*, 10.1002/2014GL060865.
- [29] Nilson, R. H., E. W. Peterson, K. H. Lie, N. R. Burkhard, & J. R. Hearst (1991). Atmospheric pumping: A mechanism causing vertical transport of contaminated gases through fractured permeable media, *J. Geophys. Res.*, 96, 21,933–21,948.
- [30] Pazdniakou, A., Mourzenko, V.V., Thovert, J.-F., Adler, P.M., & Pili, E. (in preparation). Single phase flow, heat transfer and tracer transport to the atmosphere from an underground chimney through a fractured porous medium.
- [31] Pili, E., Bureau, S., Perrier, F., Patriarche, D., Charlet, L., Adler, P.M. and Richon, P.

- (2008). Reactive Transport and residence times in unsaturated fractured rocks from field-scale experiments, *Adsorption to Geomedia II*, American Chemical Society, édité par M.O. Barnett and D.B. Kent, Elsevier, Developments in Earth & Environmental Sciences, 7, 441.
- [32] Reid R. C., Prausnitz J. M., & Poling B.E. (1987). *The Properties of Gases and Liquids*, 4th ed., McGraw-Hill, Inc., New York.
- [33] Richon, P., Perrier, F., Sabroux, J.C., Trique, M., Ferry, C., Voisin, V. & Pili, E. (2005). Spatial and time variations of radon-222 concentration in the atmospheres of a dead-end horizontal tunnel. *Journal of Environmental Radioactivity*, 78, 179-198.
- [34] Sun, Y., & Carrigan, C. (2014). Modeling Noble Gas Transport and Detection for the Comprehensive Nuclear-Test-Ban Treaty. *Pure and Applied Geophysics*, 171, 735–750.
- [35] Sun, Y., Carrigan, C., & Hao, Y. (2015). Radioxenon production and transport from an underground nuclear detonation to ground surface. *Pure and Applied Geophysics*, 172, 243–265.
- [36] Sun Y., & Carrigan, C.R. (2016). Thermally driven advection for radioxenon transport from an underground nuclear explosion. *Geophysical Research Letters* 43(9),4418–4425, 10.1002/2016GL068290.
- [37] Sweby, P.K. (1984). High resolution schemes using flux limiters for hyperbolic conservation laws. *SIAM Journal on Numerical Analysis*, 21, 995–1011.
- [38] Topin, S., Gross, P., Achim, P., Generoso, S., Cagniant, A., Delaune, O., Morin, M., Philippe, T., Fontaine, J.-P., Moulin, C., Douysset, G. and Le Petit, G. (2020). 6 months of radioxenon detection in western Europe with the SPALAX-New generation system - Part1: Metrological capabilities. *Journal of Environmental Radioactivity* 225 106442.
- [39] van Genuchten, M. T., (1980). A closed-form equation for predicting the hydraulic conductivity of unsaturated soils. *Soil Sci. Soc. Am. J.* 44, pp. 892–898.

Parameter	CBC	CIDZ
Domain size [m <sup>3</sup> ]	100×100×400	200×200×650
Damaged zone size [m <sup>3</sup> ]	defined by $V_c = 5 \times 10^5$	100×100×200
Porous medium permeability $K_m$ [m <sup>2</sup> ]	$8 \times 10^{-14}$	$10^{-16}$
Chimney permeability $K_c$ [m <sup>2</sup> ]	instant equilibrium	$8.33 \times 10^{-8}$
Porous medium porosity $\varepsilon_m$	0.05	0.01
Chimney porosity $\varepsilon_c$	1	0.29
Number of fractures	147	192
Fracture aperture b [m]	$10^{-3}$	$10^{-3}$
Liquid viscosity $\mu_w$ [Pa s <sup>-1</sup> ]	$10^{-3}$	$10^{-3}$
Gas viscosity $\mu_n$ [Pa s <sup>-1</sup> ]	$2 \times 10^{-5}$	$2 \times 10^{-5}$
Solid density $\rho_s$ [kg m <sup>-3</sup> ]	2700	2700
Solid heat capacity $c_s$ [J kg <sup>-1</sup> K <sup>-1</sup> ]	900	900
Liquid heat capacity $c_w$ [J kg <sup>-1</sup> K <sup>-1</sup> ]	4180	4180
Dry air heat capacity $c_a$ [J kg <sup>-1</sup> K <sup>-1</sup> ]	1000	1000
Vapor heat capacity $c_v$ [J kg <sup>-1</sup> K <sup>-1</sup> ]	2000	2000
Solid conductivity $\lambda_s$ [W m <sup>-1</sup> K <sup>-1</sup> ]	2.6	2.6
Liquid conductivity $\lambda_w$ [W m <sup>-1</sup> K <sup>-1</sup> ]	0.6	0.6
Gas conductivity $\lambda_n$ [W m <sup>-1</sup> K <sup>-1</sup> ]	0.026	0.026
Vapor/air molecular diffusion $D_{mv}$ [m <sup>2</sup> s <sup>-1</sup> ]	$2.42 \times 10^{-5}$	$2.42 \times 10^{-5}$
Tracer/gas molecular diffusion $D_{mn}$ [m <sup>2</sup> s <sup>-1</sup> ]	$1.25 \times 10^{-5}$	$1.25 \times 10^{-5}$
Tracer/liquid molecular diffusion $D_{mw}$ [m <sup>2</sup> s <sup>-1</sup> ]	$1.25 \times 10^{-9}$	$1.25 \times 10^{-9}$
Gas-liquid distribution constant $K_D$	8	8
Initial tracer mass fraction inside the chimney $c_n^*$	0.1	0.1

TABLE I. Parameters and values of physical properties used in CBC and CIDZ simulations.

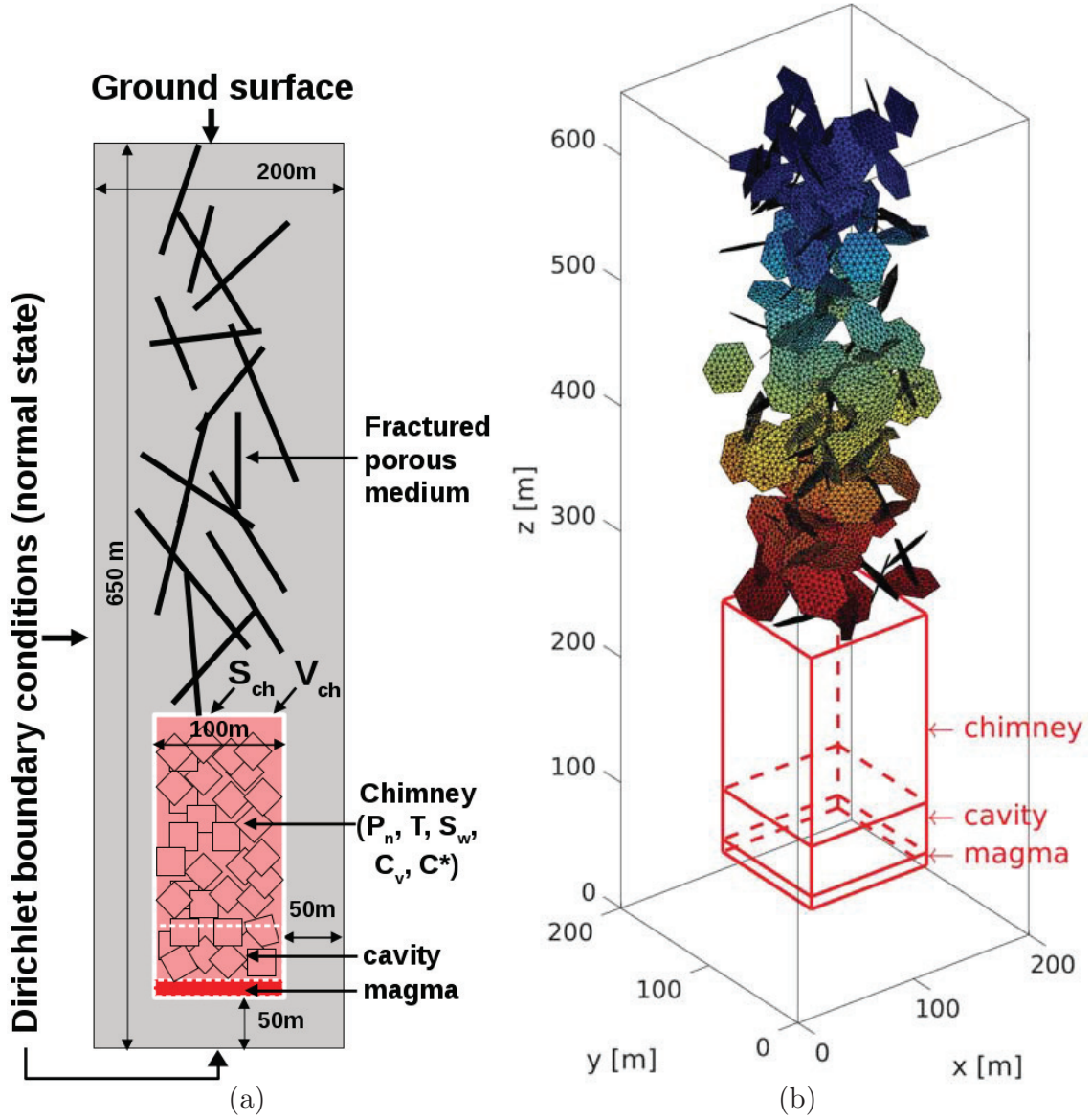


FIG. 1. The complete geometry CIDZ. The damaged zone includes the chimney, the cavity and the magma. (a) Schematized cross section of the simulation domain. (b) The percolating fracture network of 192 individual hexagonal fractures meshed with triangles inside the simulation domain. The red lines indicate the location of the chimney whose internal volume is  $V_c$  and whose surface is  $S_c$ .

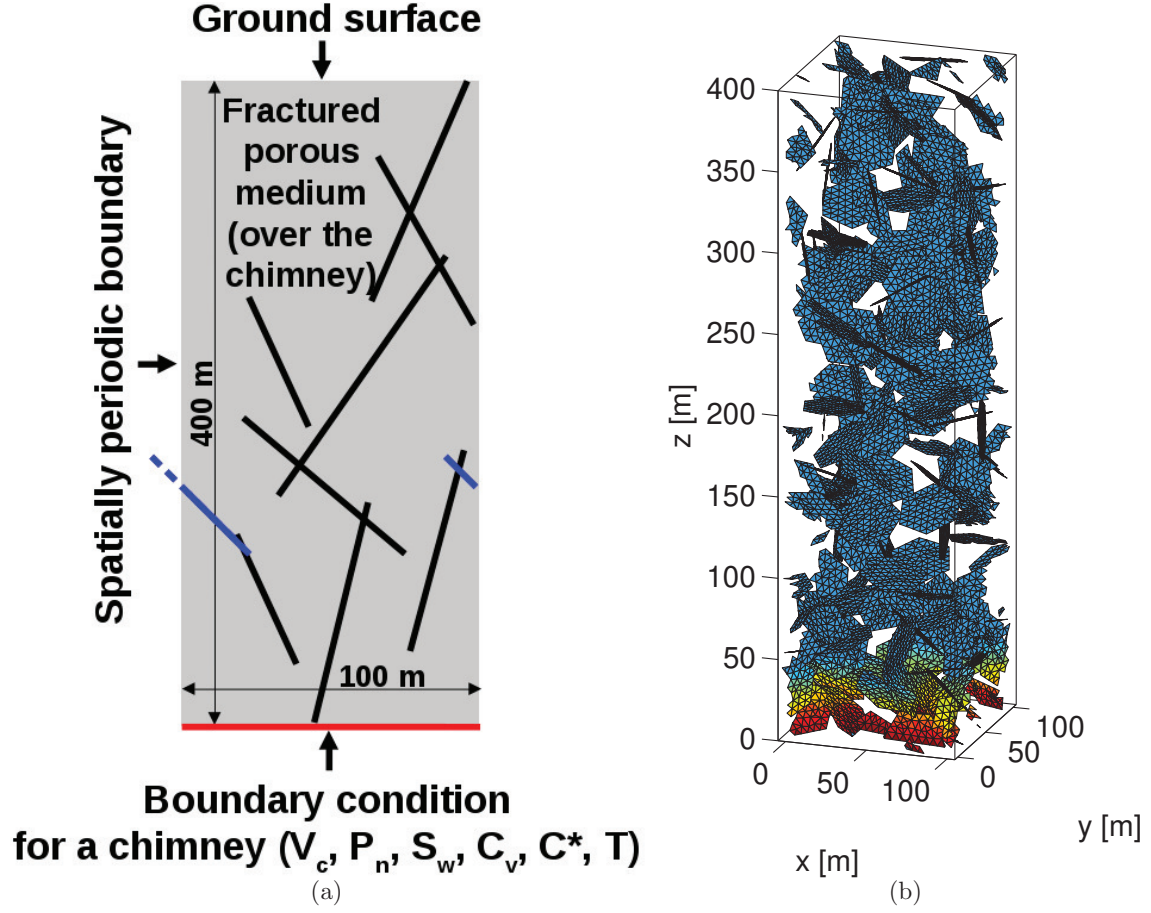


FIG. 2. The fractured porous medium configuration with boundary conditions CBC. (a) Schematized cross section of the simulation domain. (b) The percolating fracture network of 147 individual hexagonal fractures meshed with triangles inside the simulation domain.

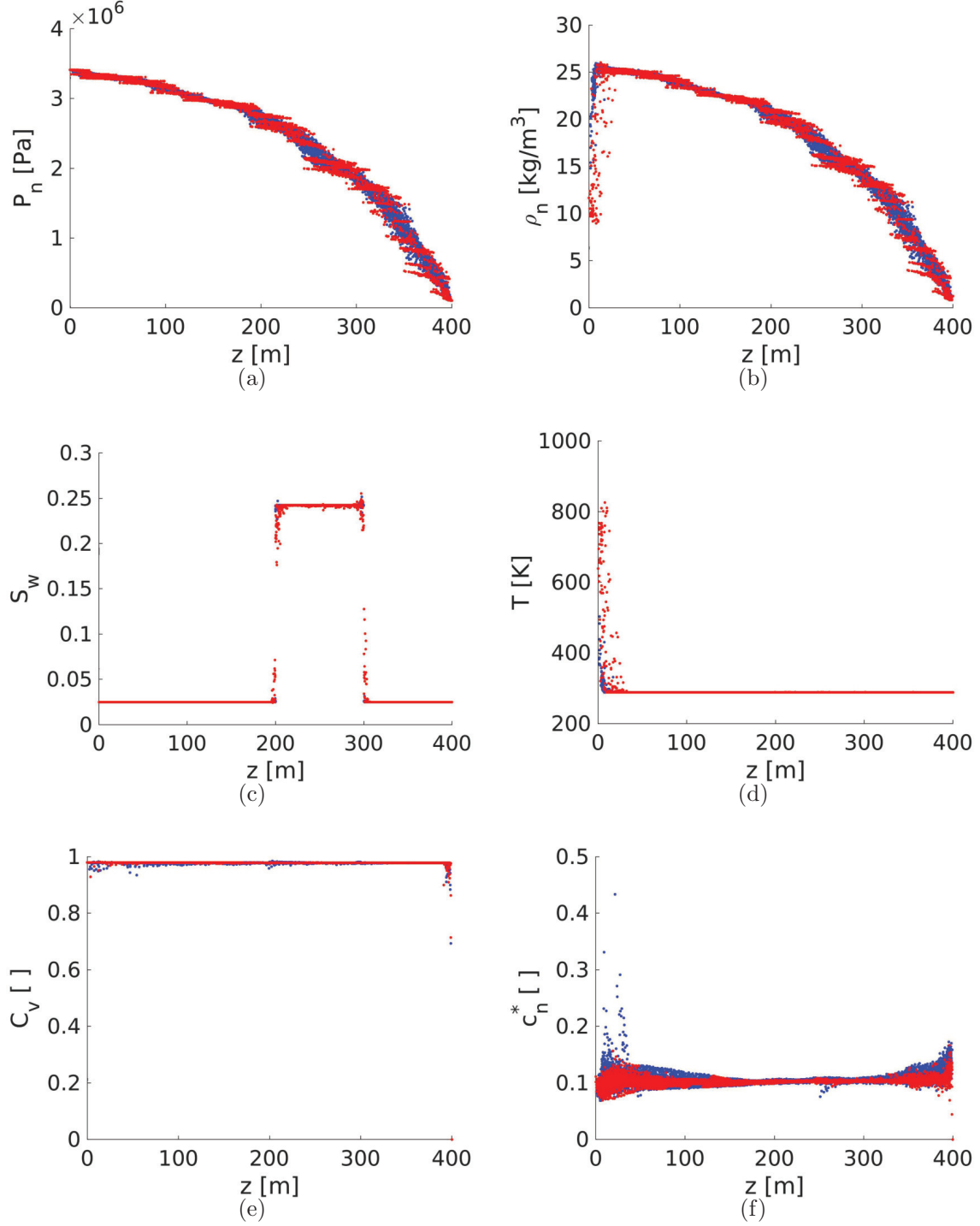


FIG. 3. CBC simulation. Two phase flow without phase change. The gas pressure (a), the gas density (b), the water saturation (c), the temperature (d), the vapor (e) and the tracer (f) mass fractions distributions inside the simulation domain at  $t = 2.68$  days. Data are for: porous medium (blue), fractures (red). The dots correspond to the values at the nodes of the tetrahedra.



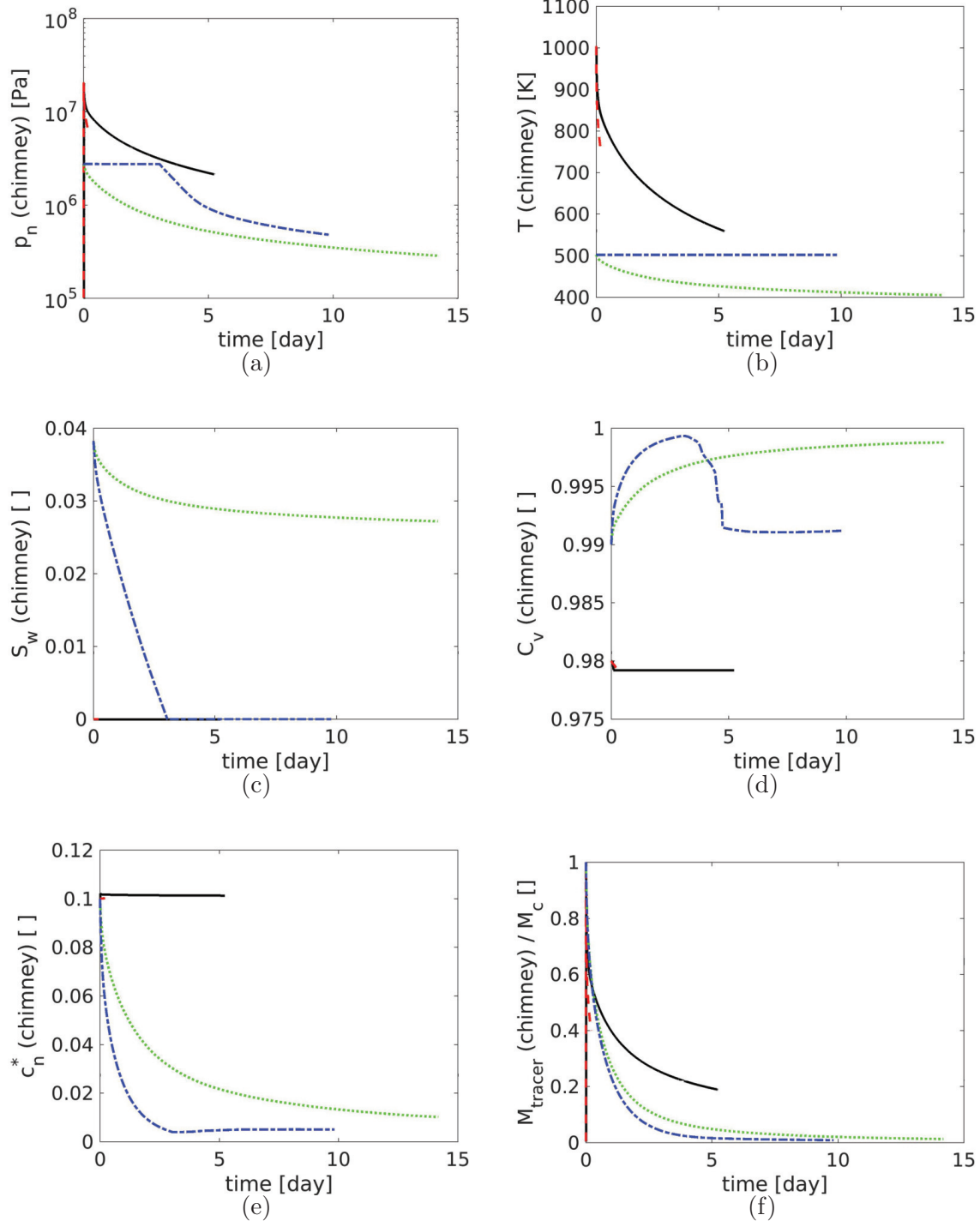


FIG. 4. CBC simulations. Evolution of the gas pressure (a), the temperature (b), the water saturation (c), the vapor (d) and the tracer (e) mass fractions, and the total tracer mass inside the chimney (f). The data are for the two phase flow without phase change (solid black lines), two phase flow with phase change (red dashed lines), two phase flow with phase change in presence of liquid water inside the chimney (green dotted lines), and two phase flow with phase change in presence of liquid water and additional heat capacity inside the chimney (blue dash-dotted lines).

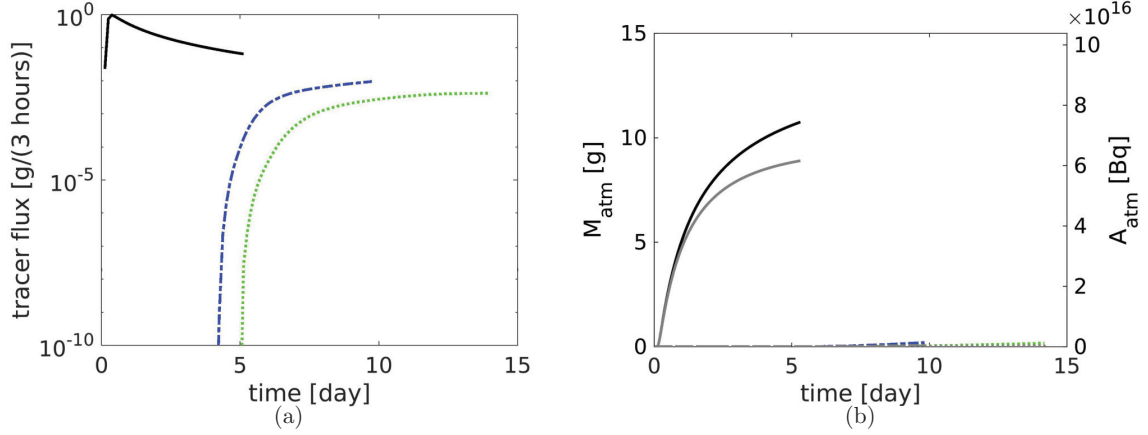


FIG. 5. CBC simulations. The total tracer flux at the ground surface (a) rescaled to  $M_c = 15$  g, and the tracer mass and the corresponding activity of  $^{133}\text{Xe}$  (grey lines) released to the atmosphere (b). The data are for the two phase flow without phase change (solid black lines), two phase flow with phase change (red dashed lines), two phase flow with phase change in presence of liquid water inside the chimney (green dotted lines), and two phase flow with phase change in presence of liquid water and additional heat capacity inside the chimney (blue dash-dotted lines).

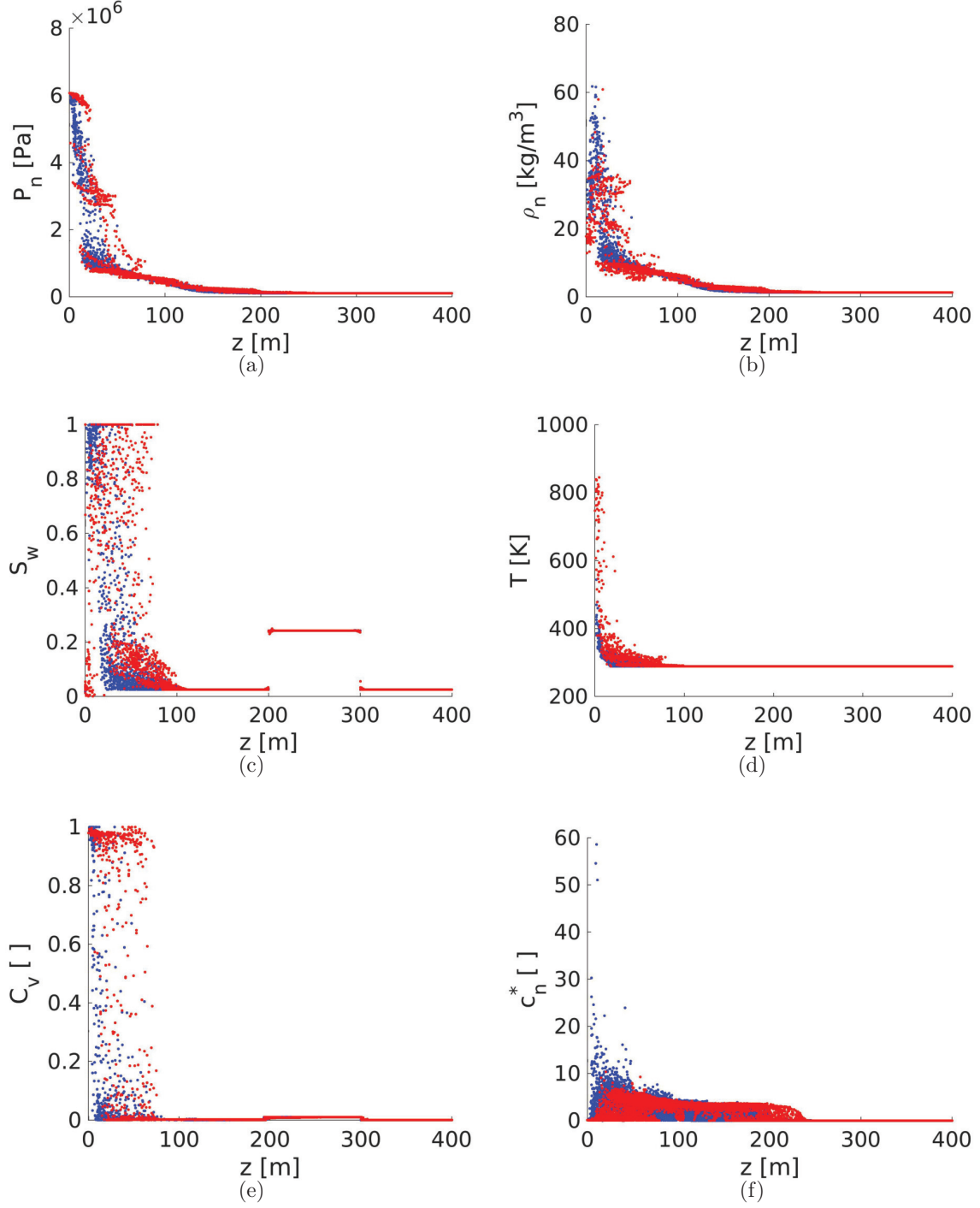


FIG. 6. CBC simulation. Two phase flow with phase change. The gas pressure (a), the gas density (b), the water saturation (c), the temperature (d), the vapor (e) and the tracer (f) mass fractions distributions inside the simulation domain at  $t = 0.2$  days. The data are for the porous medium (blue) and fractures (red).

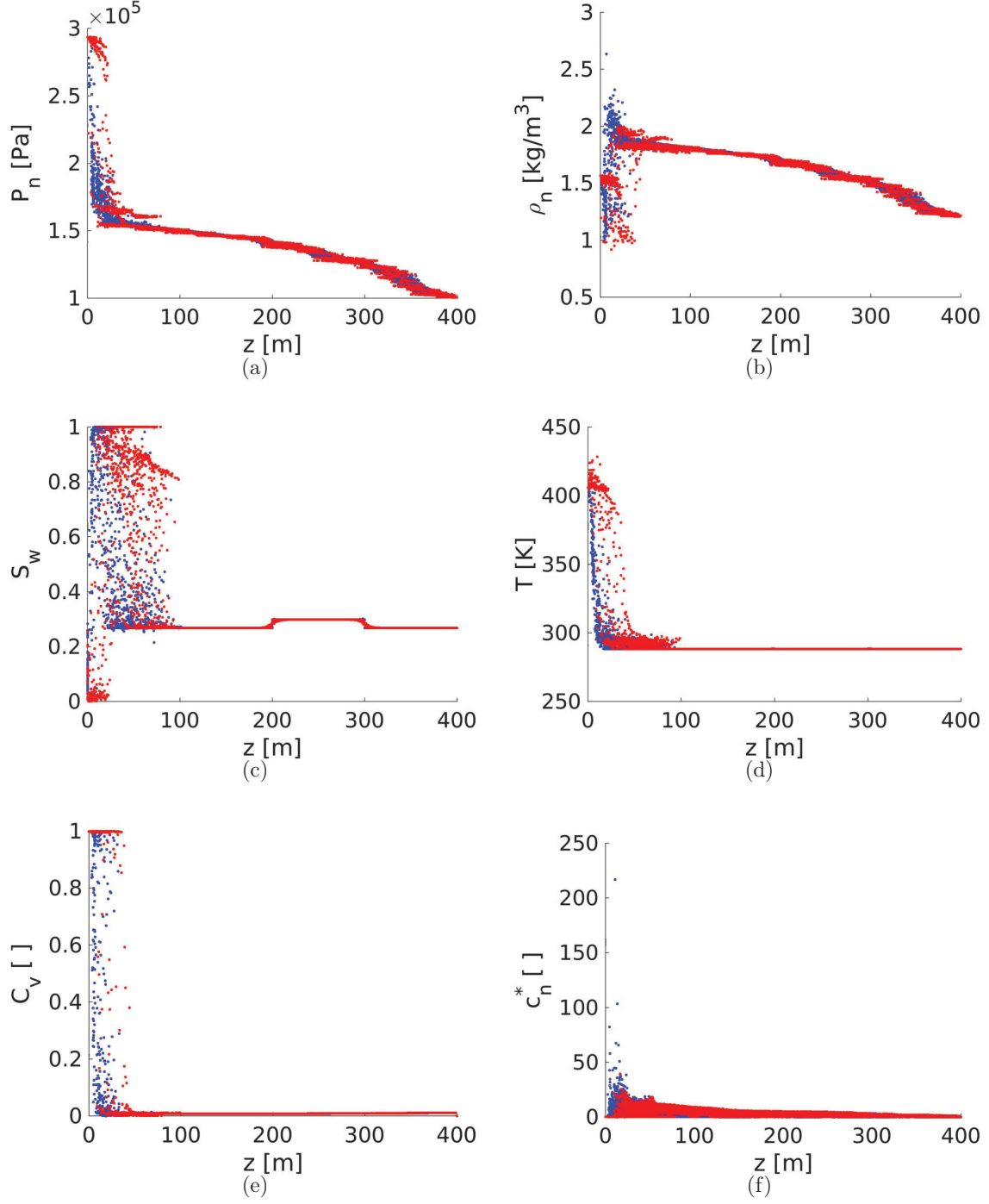


FIG. 7. CBC simulation. Two phase flow with phase change in presence of liquid water inside the chimney. The gas pressure (a), the gas density (b), the water saturation (c), the temperature (d), the vapor (e) and the tracer (f) mass fractions distributions inside the simulation domain at  $t = 13.56$  days. The data are for the porous medium (blue) and fractures (red).

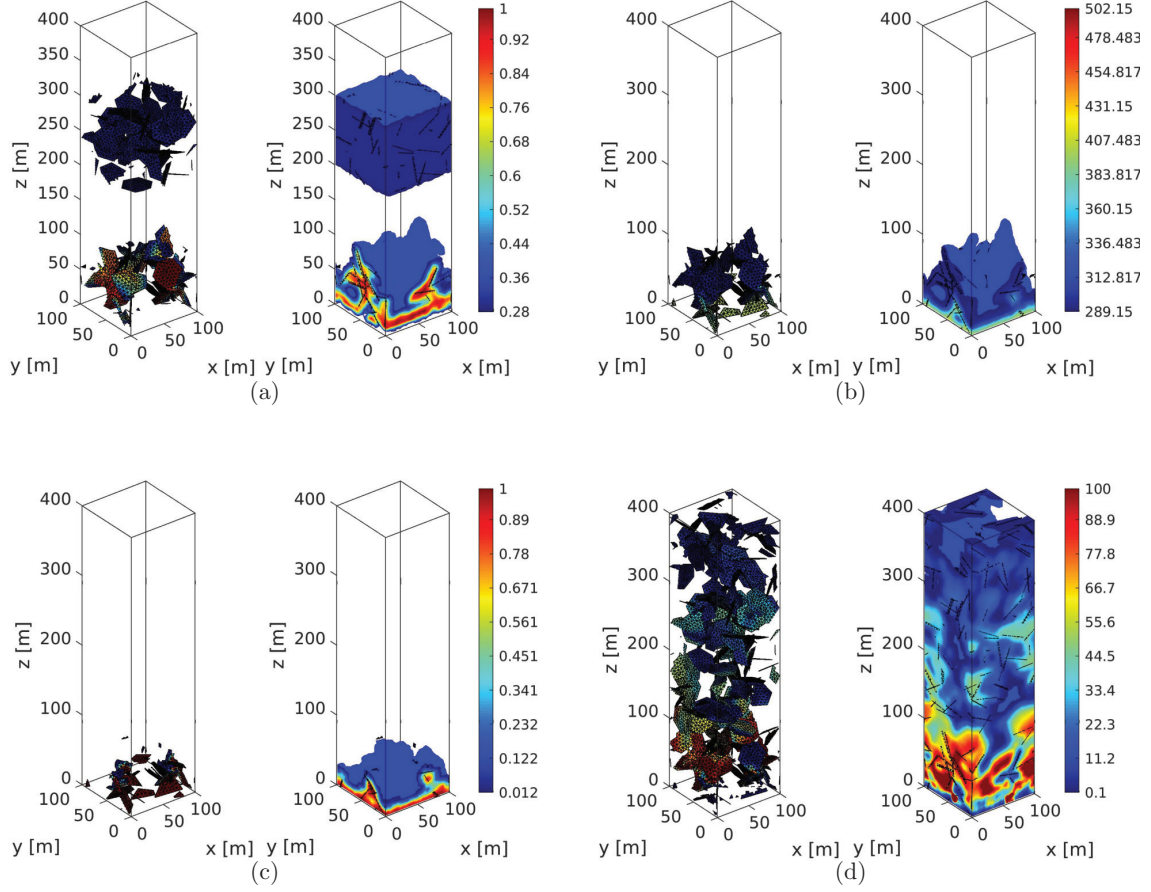


FIG. 8. CBC simulation. Two phase flow with phase change in presence of liquid water inside the chimney. Each subfigure shows the values in the fractures (left) and in the porous matrix (right). The water saturation (a), the temperature (b), the vapor (c) and the tracer (d) mass fractions distributions inside the simulation domain at  $t = 13.2$  days. Only the regions with values exceeding the threshold  $S_{w,min} = 0.28$ ,  $T_{min} = 289.15$  K,  $C_{v,min} = 0.012$ , and  $c_{n,min}^* = 0.1$ , are displayed. Note that for demonstration the upper limit of the tracer mass fraction is reduced to  $c_{n,max}^* = 100$ .

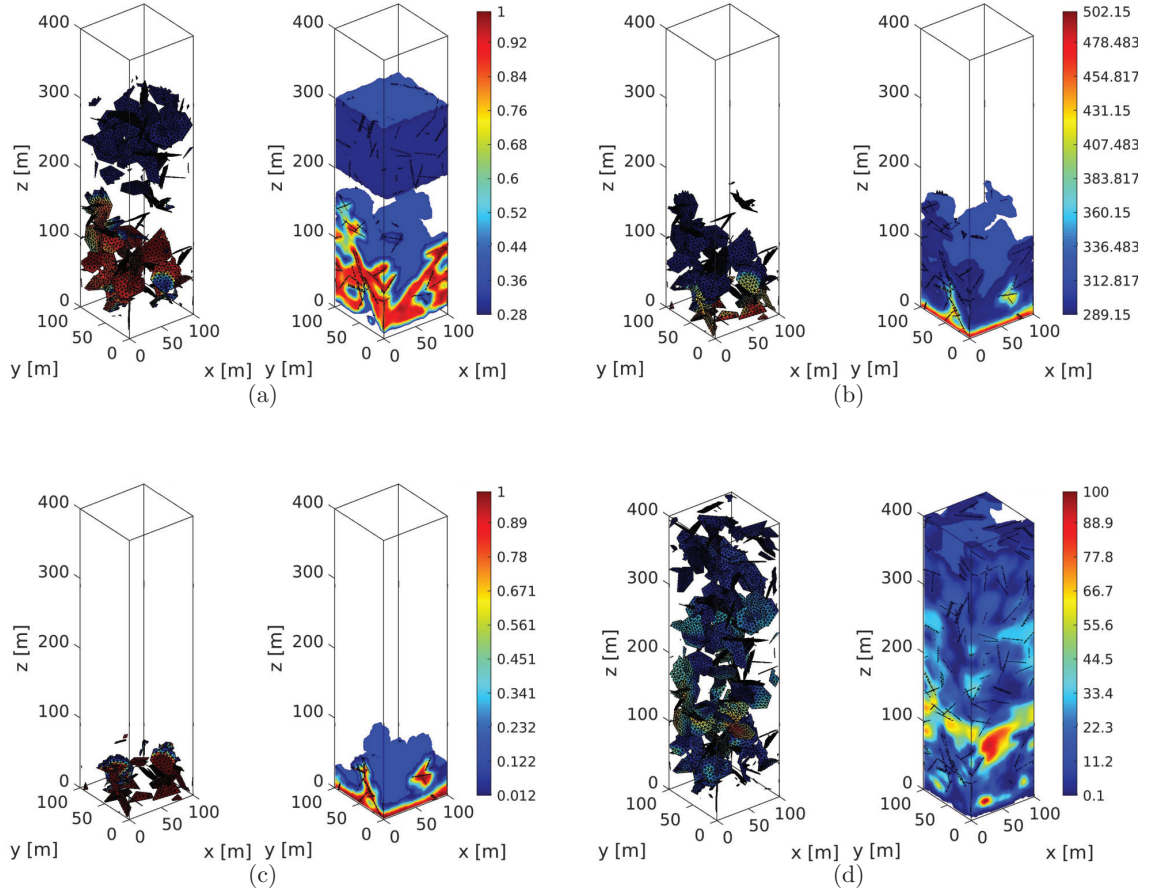


FIG. 9. CBC simulation. Two phase flow with phase change in presence of liquid water and an additional heat capacity inside the chimney. The water saturation (a), the temperature (b), the vapor (c) and the tracer (d) mass fractions distributions inside the simulation domain at  $t = 8.6$  days. Only the regions with values exceeding the threshold  $S_{w,min} = 0.28$ ,  $T_{min} = 289.15$  K,  $C_{v,min} = 0.012$ , and  $c_{n,min}^* = 0.1$ , are displayed. Note that for demonstration the upper limit of the tracer mass fraction is reduced to  $c_{n,max}^* = 100$ .

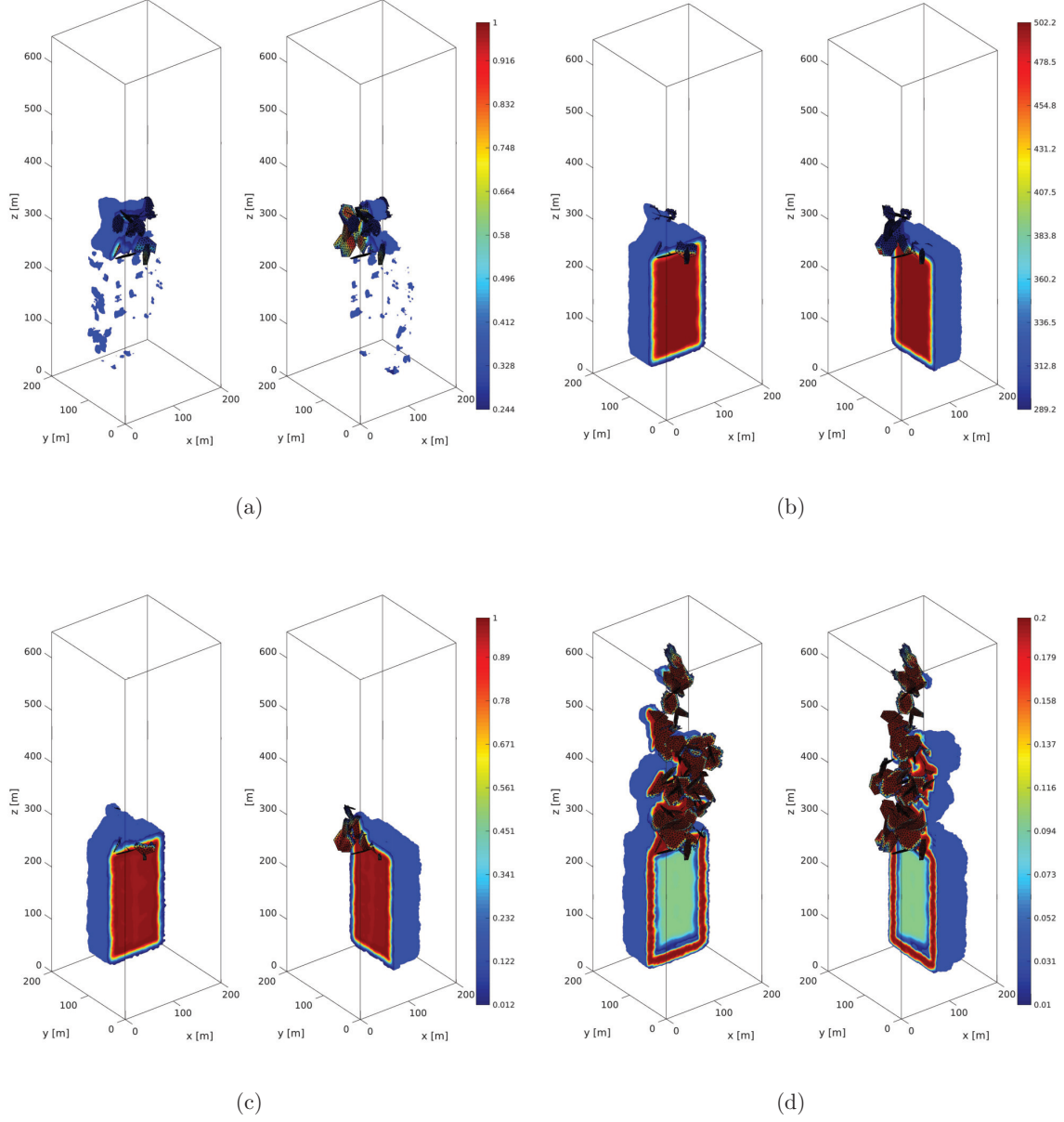


FIG. 10. CIDZ simulation without evaporation inside the uniformly heated chimney. The water saturation (a), the temperature (b), the vapor (c) and the tracer (d) mass fractions distributions inside the simulation domain at  $t = 9.96$  hours. Only the regions with values exceeding the threshold  $S_{w,min} = 0.244$ ,  $T_{min} = 289.15$  K,  $C_{v,min} = 0.012$ , and  $c_{n,min}^* = 0.01$ , are displayed. Each view contains only one half of the domain, thus allowing to see the interior of the chimney. Note that for demonstration the upper limit of the tracer mass fraction is reduced to  $c_{n,max}^* = 0.2$ .



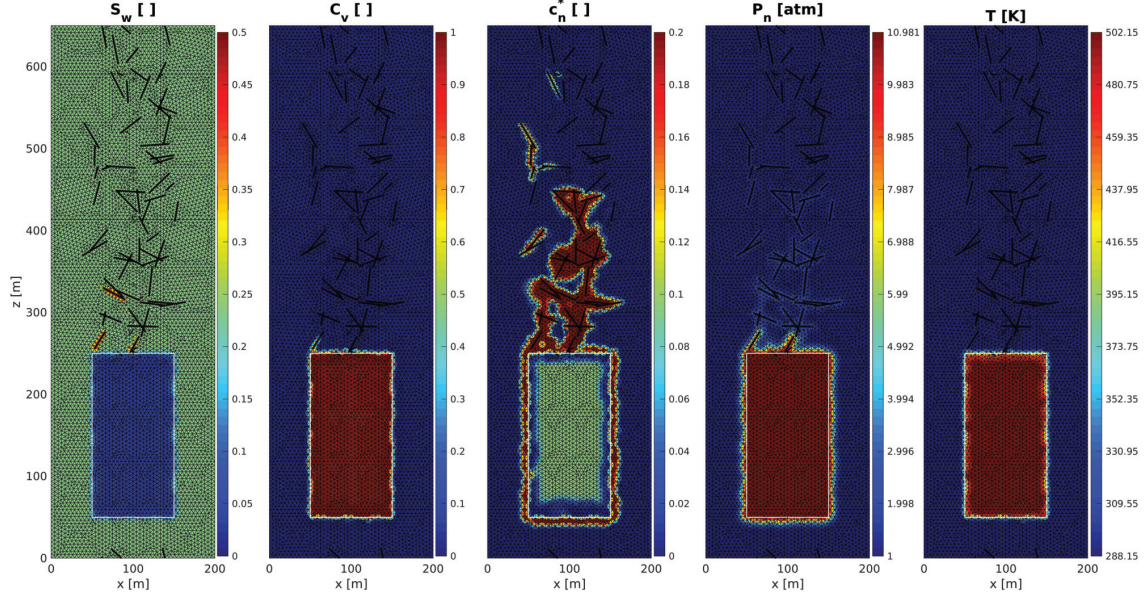


FIG. 11. CIDZ simulation without evaporation inside the uniformly heated chimney. Distribution of the water saturation, the vapor mass fraction, the tracer mass fraction, the gas pressure, and the temperature on the  $y = 100$  plane at  $t = 9.96$  hours. The white rectangle indicates the boundary of the chimney. For the sake of clarity, the upper limits of the water saturation and the tracer mass fraction plots are reduced.

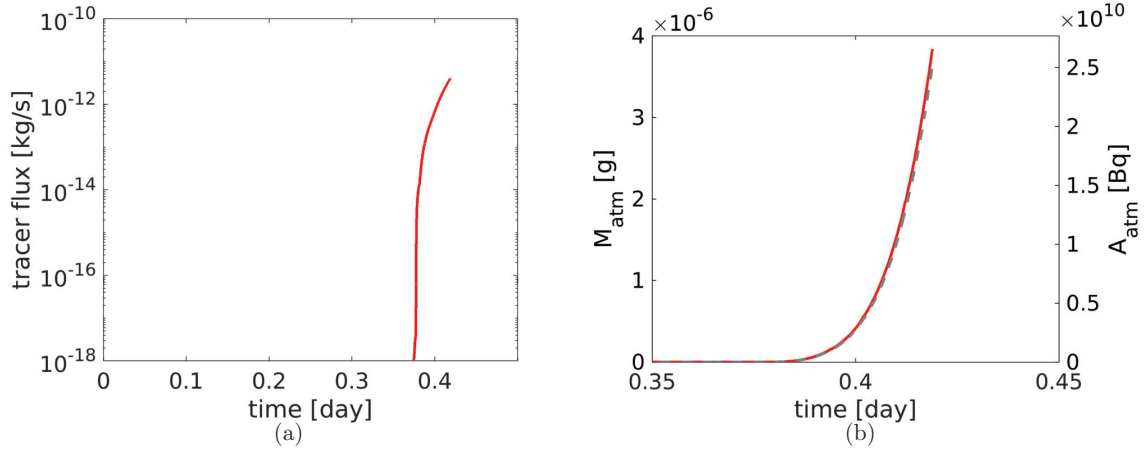


FIG. 12. CIDZ simulation without evaporation inside the uniformly heated chimney. Total tracer flux at the ground surface (a) rescaled to  $M_c = 15$  g, and the tracer mass and the corresponding activity of  $^{133}\text{Xe}$  (grey dashed line) released to the atmosphere (b).



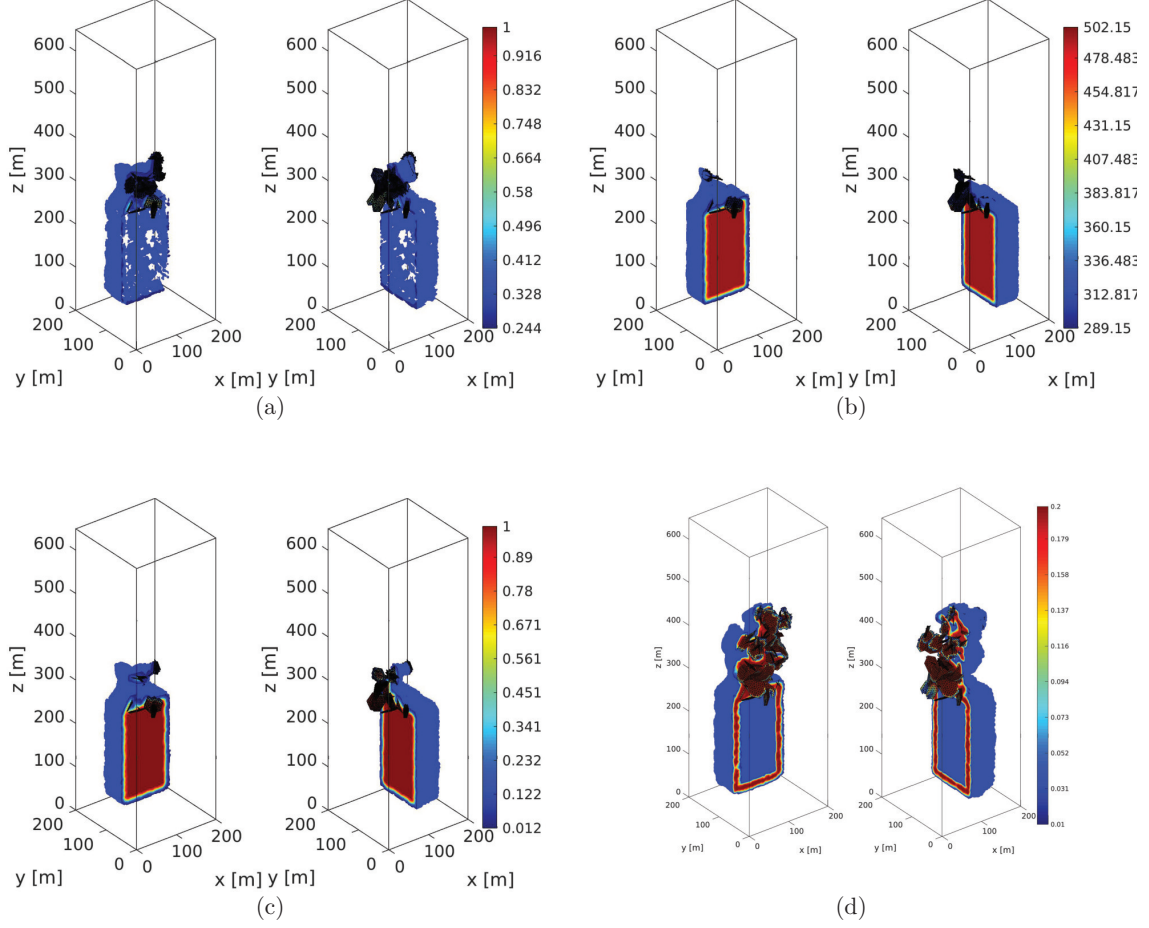


FIG. 13. CIDZ simulation with evaporation inside the uniformly heated chimney. The water saturation (a), the temperature (b), the vapor (c) and the tracer (d) mass fractions distributions inside the simulation domain at  $t = 1.71$  hours. Only the regions with values exceeding the threshold  $S_{w,min} = 0.244$ ,  $T_{min} = 289.15$  K,  $C_{v,min} = 0.012$ , and  $c_{n,min}^* = 0.01$ , are displayed. Each view contains only one half of the domain thus allowing to see the interior of the chimney. Note that for demonstration the upper limit of the tracer mass fraction is reduced to  $c_{n,max}^* = 0.2$ .

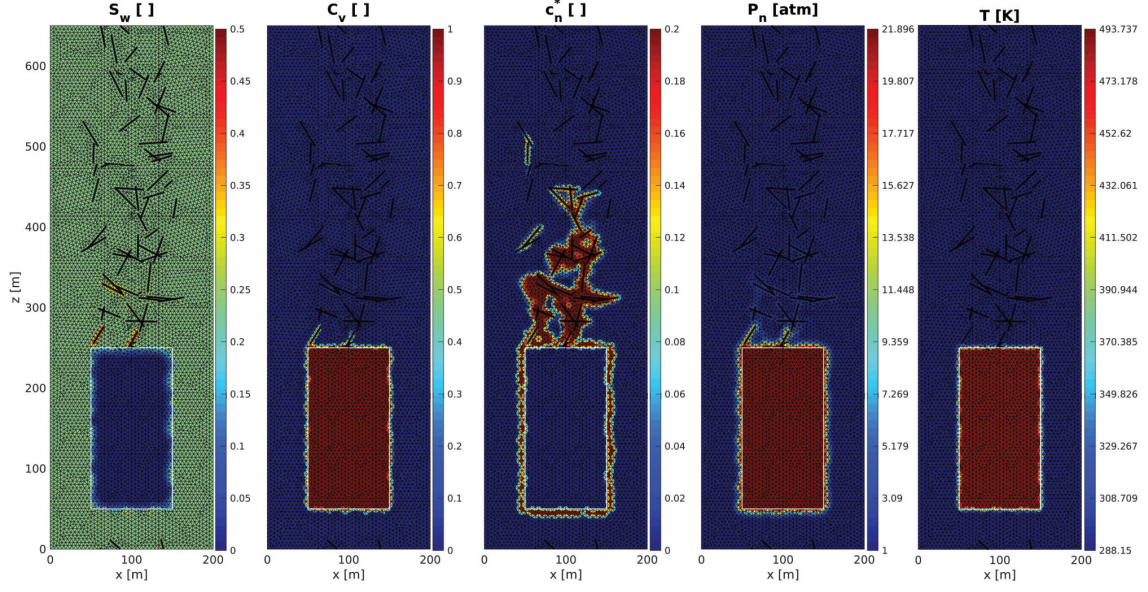


FIG. 14. CIDZ simulation with evaporation inside the uniformly heated chimney. Distributions of the water saturation, the vapor mass fraction, the tracer mass fraction, the gas pressure, and the temperature on the  $y = 100$  plane at  $t = 3.51$  hours. The white rectangle indicates the boundary of the chimney. For the sake of clarity, the upper limits of the water saturation and the tracer mass fraction plots are reduced.

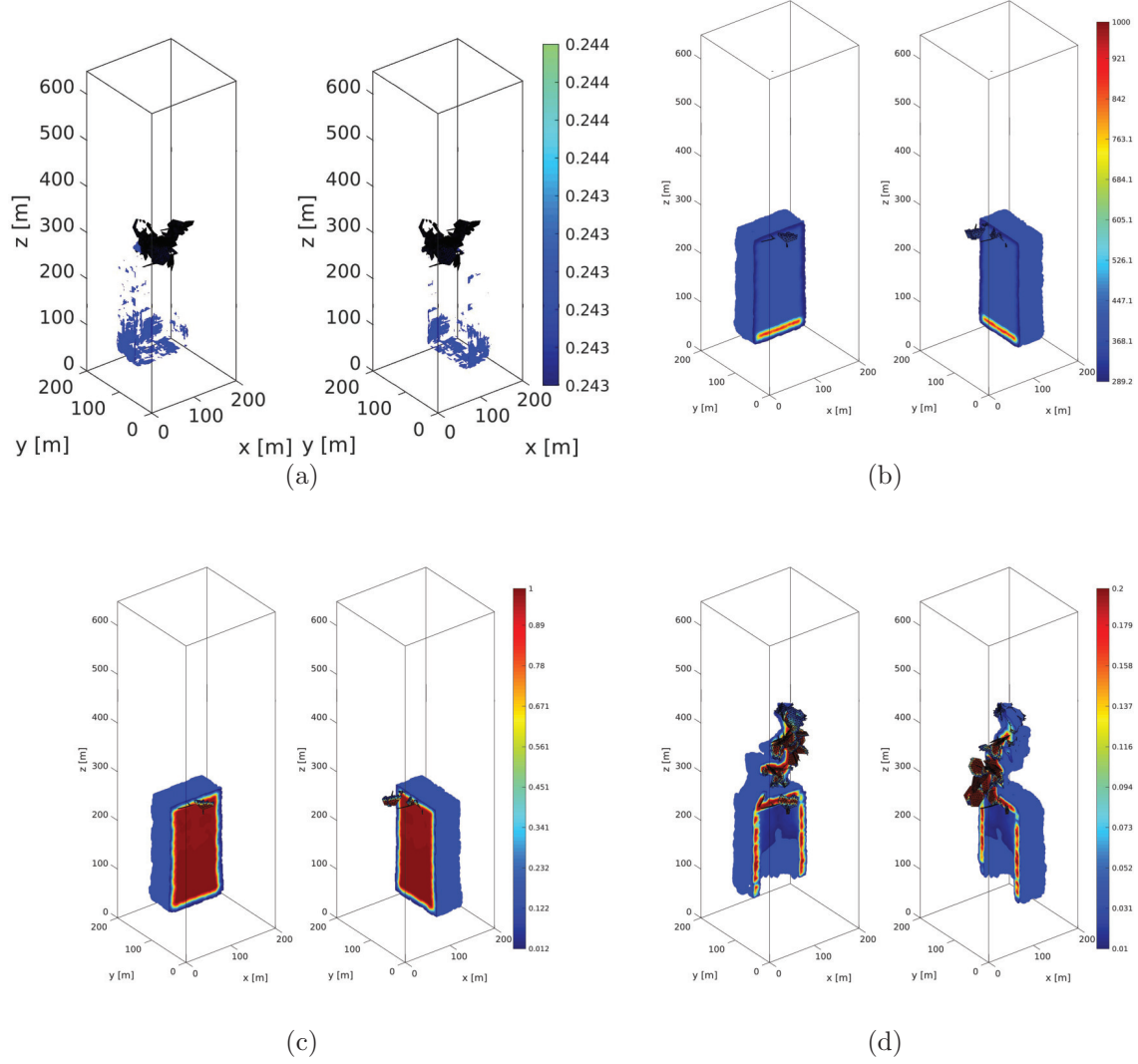


FIG. 15. CIDZ simulation with an unevenly heated chimney. The water saturation (a) at  $t = 0.54$  days, the temperature (b), the vapor (c) and the tracer (d) mass fractions distributions inside the simulation domain at  $t = 2.17$  days. Only the regions with values exceeding the threshold  $S_{w,min} = 0.243$ ,  $T_{min} = 289.15$  K,  $C_{v,min} = 0.012$ , and  $c_{n,min}^* = 0.01$ , are displayed. Each view contains only a half of the domain thus allowing to see the interior of the chimney. Note that for demonstration the upper limit of the tracer mass fraction is reduced to  $c_{n,max}^* = 0.2$ .

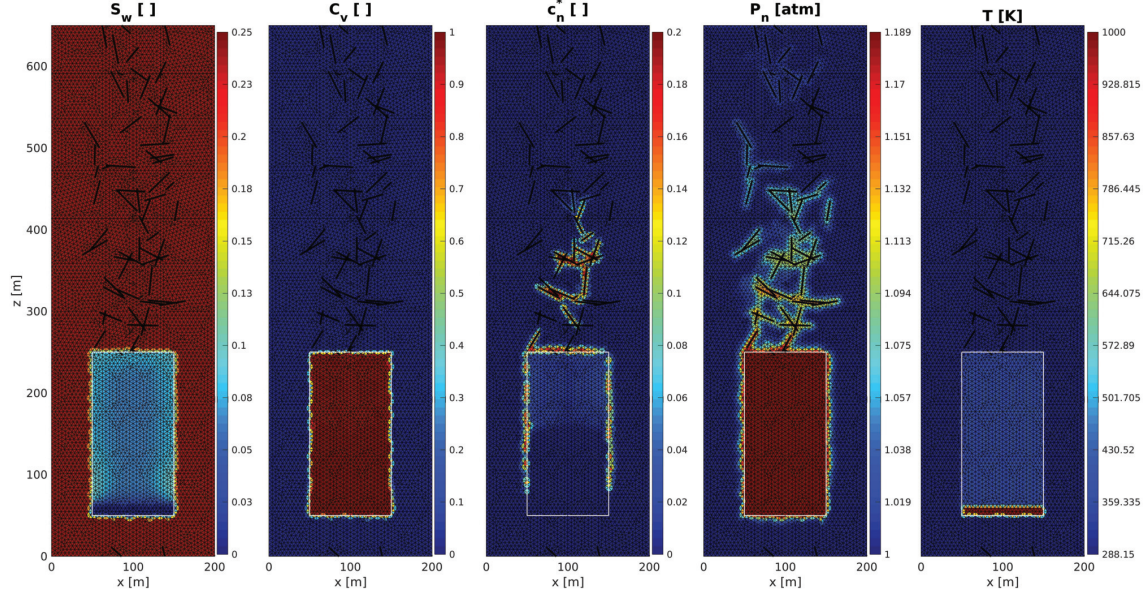


FIG. 16. CIDZ simulation with an unevenly heated chimney. Distribution of the water saturation, the vapor mass fraction, the tracer mass fraction, the gas pressure, and the temperature on the  $y = 100$  plane at  $t = 2.17$  days. The white rectangle indicates the boundary of the chimney. For the sake of clarity, the upper limits of the water saturation and the tracer mass fraction plots are reduced.

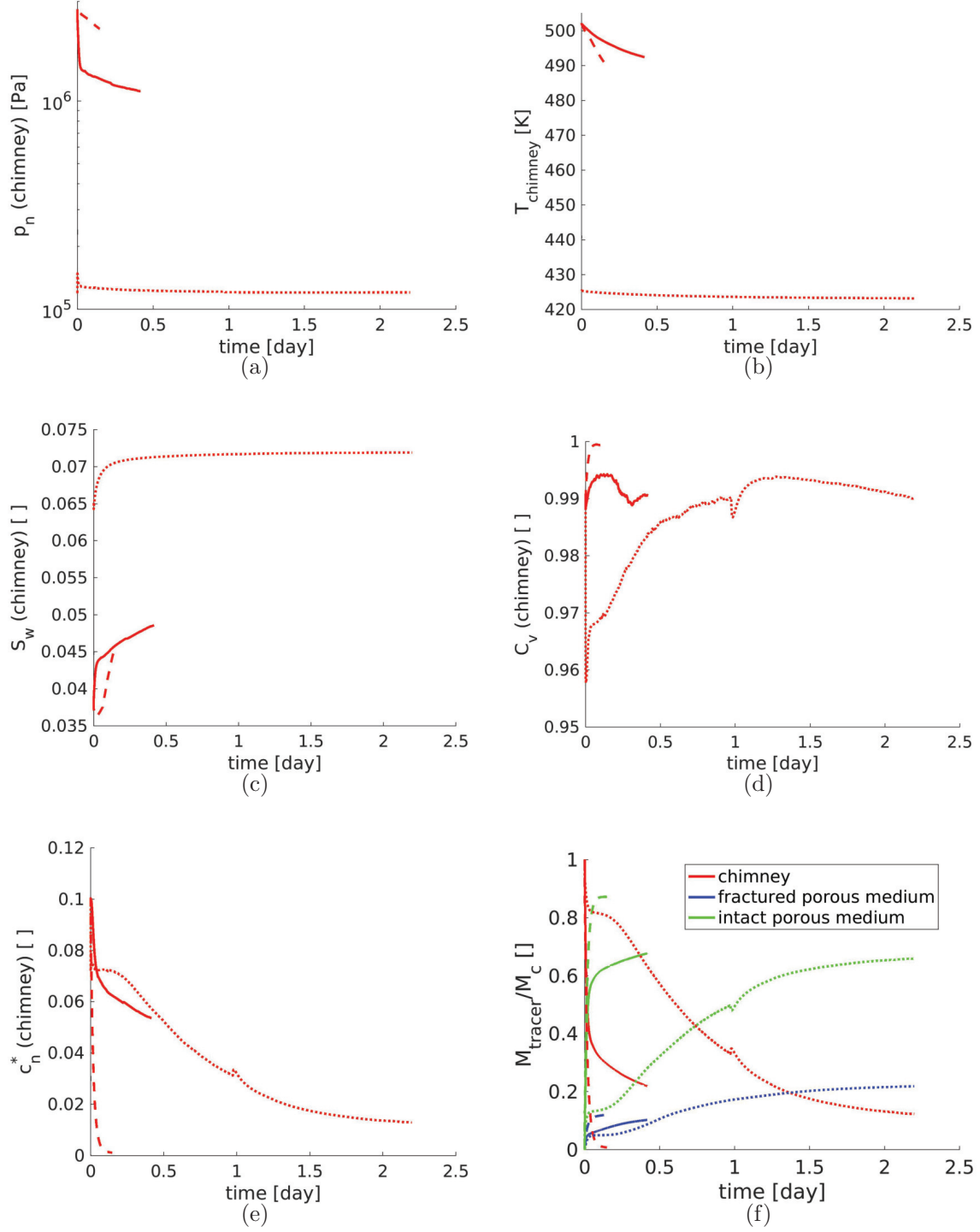


FIG. 17. CIDZ simulation. Evolution of the mean gas pressure (a), the temperature (b), the water saturation (c), the vapor (d) and the tracer (e) mass fractions inside the chimney. Evolution of the tracer mass inside the main geometrical regions (f). Data are for the uniformly heated chimney without evaporation inside the chimney (solid lines), the uniformly heated chimney with evaporation inside the chimney (dashed lines), and the unevenly heated chimney (dotted lines).



## Appendix A: Governing equations for fractures

The governing equations for fractures are gathered here.

The convection-diffusion equation is given by

$$\frac{\partial(b\varepsilon_f S_n \rho_n C_v)}{\partial t} + \nabla_S \cdot (\mathbf{q}_n \rho_n C_v) - \nabla_S \cdot (D_{mv} \bar{\Sigma}_n \rho_n \nabla_S C_v) + [\bar{\mathbf{v}}_n \rho_n C_v - D_{mv} \bar{D}_n \rho_n \nabla C_v] \cdot \mathbf{n} = -E_f \quad (\text{A1})$$

where  $\bar{\Sigma}_n$  is the effective diffusional conductivity of the fracture volume occupied by the non-wetting phase, and the last term on the left side describes the exchange between the porous matrix and the fractures. The vapor flux continuity at the fracture/porous matrix interface is ensured through the exchange term.

Then, using the same principles, a similar combined energy transport equation inside the fractures is deduced

$$\begin{aligned} \frac{\partial}{\partial t} b \{ \varepsilon_f [\rho_w (1 - S_n) h_w^* + \rho_n S_n h_n^*] + (1 - \varepsilon_f) \rho_s h_s^* \} + \nabla_S \cdot (\mathbf{q}_w \rho_w h_w^* + \mathbf{q}_n \rho_n h_n^*) \\ - \nabla_S \cdot (\Lambda_f \nabla_S T) + [\bar{\mathbf{v}}_w \rho_w h_w^* + \bar{\mathbf{v}}_n \rho_n h_n^* - \lambda_m \nabla T] \cdot \mathbf{n} \\ = R_f + b\varepsilon_f \left[ (1 - S_n) \frac{\partial p_w}{\partial t} + S_n \frac{\partial p_n}{\partial t} \right] \end{aligned} \quad (\text{A2})$$

where  $\Lambda_f [ML^2T^{-3}K^{-1}]$  is the effective thermal transmissivity of the fracture, and  $R_f [MT^{-3}]$  the energy source term inside the fracture corresponding to the phase change. The first term of the equation describes accumulation of the thermal energy; the following two terms correspond to the energy transfer due to convection and conduction. Energy flux continuity at the fracture/matrix interfaces is assured by the exchange term  $[\bar{\mathbf{v}}_w \rho_w h_w^* + \bar{\mathbf{v}}_n \rho_n h_n^* - \lambda_m \nabla T] \cdot \mathbf{n}$ .

The tracer transport equation for fractures reads as

$$\begin{aligned} \frac{\partial b\varepsilon_f \tilde{S} \tilde{C}^*}{\partial t} + \nabla_S \cdot \left( \tilde{\mathbf{q}} \tilde{C}^* - \left( D_{mw} \bar{\Sigma}_w \rho_w \nabla_S \frac{\tilde{C}^*}{K_D^{\frac{1}{2}} \rho_w} + D_{mn} \bar{\Sigma}_n \rho_n \nabla_S \frac{K_D^{\frac{1}{2}} \tilde{C}^*}{\rho_n} \right) \right) \\ + \left[ \tilde{\mathbf{v}} \tilde{C}^* - \left( D_{mw} \bar{D}_w \rho_w \nabla \frac{\tilde{C}^*}{K_D^{\frac{1}{2}} \rho_w} + D_{mn} \bar{D}_n \rho_n \nabla \frac{K_D^{\frac{1}{2}} \tilde{C}^*}{\rho_n} \right) \right] \cdot \mathbf{n} = W_f \end{aligned} \quad (\text{A3})$$

where  $\bar{\Sigma}_w$  is the effective diffusional conductivity of the fracture volume occupied by the non-wetting phase,  $W_f$  is the tracer source term inside the fractures, and the exchange term inside the brackets ensures the flux continuity at the fracture/matrix interfaces.

## Appendix B: Numerical

### 1. General

The standard approach to numerically solve the transport equations involving convection-diffusion phenomena is the finite volume method which starts with the discretization of the simulation domain by a conforming mesh whose elements do not exceed a prescribed size  $\delta$ . First, the generated fracture network is meshed with triangles (Huseby et al, 1997; Adler et al, 2012). Then, based on this initial mesh, the rest of the space is meshed with tetrahedra (Bogdanov et al, 2003 a and b). This set of data is then rearranged in order to be more efficiently processed by the parallel code based on OpenMP.

The partial differential equations are discretized following the finite volume methodology. The variables of interest such as pressure, temperature, and concentration are defined at the mesh nodes, i.e., the vertices of tetrahedra and triangles.

The discretized equations are solved by the conjugate gradient method. For the non-linear fluid flow equations, an iterative approach based on the Picard iterative method is employed. In order to limit numerical dispersion, the convection-diffusion equations are discretized with a flux limiting scheme based on a SuperBee function (Harten, 1993; Sweby, 1984) generalized to three dimensions.

### 2. Time discretization

The code works with a variable time step which evolves during the simulation to meet the imposed numerical stability and accuracy criteria. Usually, the time step  $\delta t$  is much larger than  $t_{0.5,\alpha}$ , which means that  $\left[1 - 2^{-\frac{\delta t}{t_{0.5,\alpha}}}\right]$  in (28) is very close to 1 and that the original source terms are effectively retrieved. However, when the code experiences some convergence difficulties during the simulation (for example because of a complicated physical situation), the time step is progressively reduced. Unfortunately, in this situation, the original source terms actually grow because of the  $\delta t^{-1}$  factor. On the other hand, the factors within brackets decrease in such situations thanks to the  $\left[1 - 2^{-\frac{\delta t}{t_{0.5,\alpha}}}\right]$  factor, and the choice of  $t_{0.5,\alpha}$  permits to effectively control this process. It may be also possible to use  $t_{0.5,\alpha}$  in order to introduce an additional time scale parameter into the evaporation/condensation source term.

### 3. Saturations close to zero

When  $S_w$  goes to zero, i.e. when for instance the chimney becomes completely dry, (19) may create some difficulties since  $p_c$  is expected to become infinite. This does not happen in our formulation since the evaporation rates provided by (28) are very high, especially for high temperatures. During the simulation, the wetting phase disappears when  $S_w$  approximately reaches  $10^{-6}$  ( $p_{ca} \approx 10^9$  Pa). At this point, the source term (28) evaporates all the wetting phase present inside a control volume during one time step. Thus, the problem of infinite capillary pressure values is avoided.